ATLAS PUB Note

ATL-PHYS-PUB-2020-023

15th September 2020

Study of top-quark pair modelling and uncertainties using ATLAS measurements at $\sqrt{s}$=13 TeV

The ATLAS Collaboration

The modelling of top-quark pair production by the ATLAS collaboration utilises recent Monte Carlo generators with next-to-leading order precision in QCD and matched to a parton shower. Various next-to-leading order and multileg generators and their settings are explored and their predictions are compared to recent ATLAS measurements in three different top-quark pair decay channels using an integrated luminosity of 36.1 fb^{-1}of $\sqrt{s}$ = 13 TeV pp collision data. The use of alternative generators and settings for the top-quark modelling uncertainty are explored, with particular focus on uncertainties related to the matching scale and algorithms, the parton shower, and the initial-state radiation.

ATL-PHYS-PUB-2020-023
15 September 2020

Contents

1 Introduction

Reliable predictions for the production of a top-quark pair are important for precision measurements in the top sector as well as for many searches for new physics at the Large Hadron Collider (LHC), for which $t\bar{t}$ production often constitutes a dominant background. The ATLAS Collaboration has previously documented the choice of Monte Carlo (MC) generator parameters and samples dedicated to improve the description of top-quark kinematics in Refs [1–5]. The aim of this note is to discuss the top-quark modelling with an emphasis on the evaluation of the NLO+PS matching algorithm uncertainty and the introduction of an alternative setup with respect to Powheg+Pythia 8 [6–10], based on Sherpa [11]. MC samples with new configurations are compared to the standard samples used by the ongoing Run 2 analyses. The comparisons are made using 36.1 fb^{-1} of published unfolded $t\bar{t}$ data at $\sqrt{s}$=13 TeV.

The different MC generators that have been studied are discussed in Section 2, they are followed by the description of the current top pair modelling uncertainties in Section 3. A short overview of the analyses used in this note to compare the new MC predictions to the unfolded data distributions is provided in Section 4 and the description of the shown observables is detailed in Section 5. The top-quark pair modelling uncertainties are then investigated; the NLO+PS matching algorithm uncertainty is detailed in Section 6, the parton shower is described in Section 7 and different settings in the initial-state radiation uncertainty are discussed in Section 8. New settings for the showering of Powheg+Pythia 8 are discussed in Section 9 and the setup based on Sherpa is described in Section 10. Finally, conclusions are given in Section 11.

2 Monte Carlo samples

In the following, a description of the inclusive $t\bar{t}$ samples used in the studies presented in this note is given.

The nominal MC sample used in ATLAS to model $t\bar{t}$ production uses the hvq program [6] in the PowhegBox v2 [6–9] generator which provides matrix elements at next-to-leading order (NLO) for top-quark pair production in the strong coupling constant, α_S . The `NNPDF3.0NLO` [12] parton distribution functions (PDFs) are used in the matrix element. The functional form of the renormalisation and factorisation scale is set to the default scale $\sqrt{m_{\text{top}}^2 + p_{\text{T}}^2}$, which is calculated from the top-quark mass, m_{top}, and the transverse momentum before radiation. The h_{damp} parameter that controls the p_{T} of the first additional emission beyond the Born configuration is tuned to $1.5m_{\text{top}}$ [3, 13]. The events are interfaced with Pythia8.230 [10] for the parton shower and hadronisation, using the A14 set of tuned parameters [13] and the `NNPDF2.3lo` set of PDFs [14]. This sample is referred to as PWG+PY8 in the plots.

The nominal sample is compared to a sample produced using the same Powheg settings and interfaced with Herwig7.0.4 [15, 16], using the H7UE set of tuned parameters [16] and the `MMHT2014LO` PDF set [17]. This sample is referred to as PWG+H7.0 in the plots. A similar sample is interfaced with Herwig7.1.3 [15, 16], using the Herwig7.1 default set of tuned parameters [16, 18] and the `MMHT2014LO` PDF set [17]. The main differences between the two Herwig7 versions are the introduction of the NLO corrections in the $t\bar{t}$ decay and the re-tune of the minimum-bias. This sample is referred to as PWG+H7.1 in the plots.

An alternative sample of $t\bar{t}$ events is produced with MadGraph5_aMC@NLO+Pythia8. For the calculation of the hard-scattering, MadGraph5_aMC@NLO v2.6.0 [19] with the `NNPDF3.0NLO` [12] PDF set is used. The functional form of the renormalisation and factorisation scale is set to the dynamic scale $m_{\text{top}} + 0.5 * (p_{\text{y,top}}^2 + p_{\text{x,top}}^2)$. The shower starting scale has the functional form $\mu_{\text{q}} = H_{\text{T}}/2$ [2], where H_{T} is defined as the scalar sum of the p_{T} of all outgoing partons. The renormalisation and factorisation scale choice is the same as for the nominal Powheg+Pythia 8 setup. Top quarks are decayed at leading-order (LO) using MadSpin [20, 21] to preserve spin correlations. The events are interfaced with Pythia8.230 [10], using the A14 set of tuned parameters [13] and the `NNPDF2.3lo` set of PDFs [14]. This sample is referred to as MG5_aMC@NLO+PY8* in the plots.

An additional sample was generated with the same MadGraph5_aMC@NLO v2.6.0 settings which was interfaced with Herwig7.1.3 [15, 16], using the Herwig7.1 default set of tuned parameters [16] and the `MMHT2014LO` PDF set [17]. This sample is referred to as MG5_aMC@NLO+H7.1 in the plots.

Additional samples of $t\bar{t}$ events are produced with the Sherpa 2.2.8 [11] generator using NLO-accurate matrix elements for up to one additional parton, and LO-accurate matrix elements for up to four additional partons. The additional parton emissions are matched and merged with the Sherpa parton shower based on Catani-Seymour dipole factorisation [22, 23] using the MEPS@NLO prescription [24–27]. The virtual QCD correction for matrix elements at NLO accuracy are provided by the OpenLoops 2 library [28–31]. Samples are generated using the `NNPDF3.0nnlo` set [12], along with the dedicated set of tuned parton-shower parameters developed by the Sherpa authors. The default showering starting scale is defined as the maximum transverse mass squared of the outgoing particles in the core process. The Sherpa sample includes approximate NLO EW_{virt} corrections [32–34]. The scale used for the multi-jet merging (Q_{cut}) is set to 30 GeV. The calculation is performed in the G_μ scheme, ensuring an optimal description of pure electroweak interactions at the electroweak scale.

The EvtGen v1.6.0 program [35] was used to simulate the decay of bottom and charm hadrons in all samples except those generated using Sherpa.

All samples are normalised to the cross-section prediction at next-to-next-to-leading order (NNLO) in QCD including the resummation of next-to-next-to-leading logarithmic (NNLL) soft-gluon terms calculated using Top++2.0 [36–42]. For proton–proton collisions at a centre-of-mass energy of $\sqrt{s}$ = 13 TeV, this cross-section corresponds to $\sigma(t\bar{t})_{\text{NNLO+NNLL}}$ = 832 ± 51 fb using a top-quark mass of m_{top} = 172.5 GeV. The uncertainties on the cross-section due to PDF and α_S are calculated using the PDF4LHC prescription [43] with the MSTW2008 68% CL NNLO [44, 45], CT10 NNLO [46, 47] and NNPDF2.3 5f FFN [14] PDF sets, and are added in quadrature to the scale variations.

A summary of the matrix element (ME), parton shower (PS) and underlying event (UE) settings for each of the generator samples studied here is presented in Table 1.

Sample Name	ME Gen.	PS/UE Gen.	ME PS/UE PDF	PS Tune	Matching Merging
PWG+PY8	PowhegBox v2_r3026	Pythia8 8.230	NNPDF3.0NLO NNPDF2.3lo	A14	Powheg (h_{damp}=1.5 m_{top})
MG5_aMC@NLO+ +PY8*	MadGraph5 _ aMC@NLO v2.6.0	Pythia8 8.230	NNPDF3.0NLO NNPDF2.3lo	A14	MC@NLO
MG5_aMC@NLO +H7.1	MadGraph5 _ aMC@NLO v2.6.0	Herwig7 7.1.3	NNPDF3.0NLO MMHT2014LO	Herwig7.1 default	MC@NLO
PWG+H7.0	PowhegBox v2_r3026	Herwig7 7.0.4	NNPDF3.0NLO MMHT2014LO	H7UE	Powheg (h_{damp}=1.5 m_{top})
PWG+H7.1	PowhegBox v2_r3026	Herwig7 7.1.3	NNPDF3.0NLO MMHT2014LO	Herwig7.1 default	Powheg(h_{damp}=1.5 m_{top})
Sherpa	Sherpa 2.2.8	Sherpa	NNPDF3.0nnlo	default	s-MC@NLO MEPS@NLO (Q_{cut} = 30 GeV)

Table 1: ME and PS/UE generator settings for each of the MC samples used for the studies presented in this note. The generator versions, the PDFs used for the ME and in the PS and the matching scheme are shown alongside the tune.

3 Overview of top-quark pair modelling uncertainties used in ATLAS

The theoretical modelling uncertainties on the production of top-quark pairs in hadronic interactions is broken down into several components which are assumed to be uncorrelated. The current list of modelling uncertainties used by the ATLAS Collaboration and in this note is derived from the studies described in previous notes [1–5]:

- *NLO generator*: aims to cover the difference between different approaches to perform the NLO+PS matching. Evaluated by comparing the nominal Powheg+Pythia 8 sample with MG5_aMC@NLO+Pythia 8*. This uncertainty is symmetrised.
- *PS*: aims to cover the uncertainties related to the approach used for the hadronisation and other non perturbative effects in the showering. Evaluated by comparing the nominal Powheg+Pythia 8 sample with Powheg+Herwig7.0.4. This uncertainty is symmetrised.
- *PS ISR scales*: this component accounts for the missing higher-order corrections in the hard scatter calculation and in the showering, it also includes the variation of the parameter that determines the kinematic of the leading emission. The uncertainty is evaluated by using two Powheg+Pythia 8 samples with different h_{damp} parameter values and different values of the μ_R and μ_F scales in the hard scatter calculation and in the `SpaceShower` part of the showering. It consists of an *up* and *down* variation. For the *up* variation, the "Var3cUp" A14 tune weight is used and the uncertainty is evaluated by reducing $\mu_{R,F}$ by a factor of 0.5 and the h_{damp} parameter is increased to 3 m_{top}. For the *down* variation, the "Var3cDown" A14 tune weight is used. The uncertainty is evaluated by increasing the $\mu_{R,F}$ scales by a factor of 2 and the h_{damp} parameter was set to the nominal value (1.5 m_{top}).
- *ME PDF*: Evaluated by combining the 100 eigenvector variations of the `NNPDF` PDF set.

These uncertainties are evaluated from the difference between samples at particle-level, which is then applied as a relative difference with respect to the nominal Powheg+Pythia 8 sample.

4 Description of analyses

The MC generators considered in this study are compared to three ATLAS measurements of top-quark pair production. The measurements were performed using pp collisions at $\sqrt{s}$=13 TeV and a luminosity of 36.1 fb^{-1}, in all the decay channels of the $t\bar{t}$ system. This is a significant difference and improvement with respect to previous notes as those studies relied on measurements at a lower centre-of-mass energy or obtained using only 2015 data, corresponding to 3.2 fb^{-1} [1–4]. The considered measurements were performed at particle-level and unfolded to a fiducial phase-space designed to minimize the extrapolation between detector-level and particle-level. The particle-level objects are designed to be similar to the detector-level ones, employing only stable particles (mean lifetime $\tau > 30$ ps). The leptons used in the analyses are required to not originate from hadrons, either through a τ-lepton decay or directly. Consequently only e and μ originating from W decay, directly or through a τ decay, are considered. The e and μ considered are dressed by including all photons not originating from hadron decays, within a cone $\Delta R = 0.1$ around the bare lepton. The studies shown in this document have been performed with Rivet 2.7 [48] and the analyses used are listed below.

- **ATLAS_2019_I1750330: Measurements of top-quark pair differential and double-differential cross-sections in the ℓ+jets channel with pp collisions at $\sqrt{s}$ = 13 TeV using the ATLAS detector [49].** The cross-section is measured as a function of the kinematics of the $t\bar{t}$ system, the hadronically decaying top and additional jets in the event. The events are selected in the ℓ+jets channel, characterized by the presence of a single e or μ with $p_{\mathrm{T}} > 27$ GeV and $|\eta| < 2.5$ and at least 4 jets with $p_{\mathrm{T}} > 25$ GeV and $|\eta| < 2.5$. At least two jets are required to be ghost-matched [50] to a B-hadron with p_{T} larger than 5 GeV. The jets are reconstructed with the anti-k_{t} [51] algorithm with $R = 0.4$, using all stable particles, excluding prompt leptons and prompt neutrinos. The $t\bar{t}$ system is reconstructed using jets, leptons and missing energy with the pseudo-top algorithm [49], where the W mass is employed to reconstruct the z component of the neutrino momenta.
- **ATLAS_2019_I1759875: Measurement of the $t\bar{t}$ production cross-section and lepton differential distributions in $e\mu$ dilepton events from pp collisions at $\sqrt{s}$ = 13 TeV with the ATLAS detector [52].** In this analysis the cross-section is measured as a function of the kinematics of the two leptons produced by the $t\bar{t}$ decay. The fiducial phase-space is defined requiring exactly one e and one μ with $p_{\mathrm{T}} > 20$ GeV and $|\eta| < 2.5$. The particle-level selection does not include any requirement on the number of jets.
- **arXiv:2006.09274: Measurements of top-quark pair single- and double-differential cross-sections in the all-hadronic channel in pp collisions at $\sqrt{s}$ = 13 TeV using the ATLAS detector [53].** In this analysis the cross-section is measured as a function of the kinematics of the two top-quarks, the $t\bar{t}$ system and the additional radiation in the event. The analysis selects an all-hadronic final state by vetoing e and μ with $p_{\mathrm{T}} > 15$ GeV and $|\eta| < 2.5$, and τ leptons, not coming from hadron decays, with $p_{\mathrm{T}} > 25$ GeV and $|\eta| < 2.5$. The fiducial selection requires six anti-k_{t} ($R = 0.4$) jets with $p_{\mathrm{T}} > 55$ GeV and $|\eta| < 2.4$, additional jets are accepted with $p_{\mathrm{T}} > 25$ GeV and $|\eta| < 2.5$. Among the jets in the event exactly two are required to originate from a b-quark, defined through ghost-matching of the particle-level jet to a B-hadron with $p_{\mathrm{T}} > 5$ GeV. The two b-jets are required to be well separated, with $\Delta R(b, b) > 2.0$. The best combination of jets to reconstruct the two top-quarks, among all the permutations of light jets, is selected minimising a χ^2 that contains the two W boson masses and the difference between the masses of the two reconstructed top-quarks. Additional selection requirements are applied after the system reconstruction: the minimum χ^2 is required to be < 10, the two reconstructed top-quark masses are required to be in the window (130, 200) GeV and the maximum ΔR between a b-jet and the associated reconstructed W must be $\Delta R(b, W) < 2.2$.

These three measurements considered the uncertainties described in Section 3 by repeating the unfolding procedure separately for each of the various generator configurations and defining the uncertainty to cover the unfolding bias due to the choice of a specific model to perform the measurement. This differs from deriving the uncertainties through a direct comparison of the predictions at the particle or detector level. Due to the different procedures, the uncertainties derived from the measurements are not fully correlated with uncertainties derived through a direct comparison. As a quantitative comparison between the predictions and the data is not made here, the remaining correlations are not studied.

5 Description of observables

More than 100 distributions were measured by the analyses described in Section 4 but only a selection is shown in this note; in each of the following sections, the most sensitive observables to the effect considered

are selected. The observables used in this note are defined as follows:

- $p_{\mathrm{T}}^{t,1}$: the p_{T} of the reconstructed leading top-quark.
- $y^{t,1}$: the rapidity of the reconstructed leading top-quark.
- $p_{\mathrm{T}}{}^{t,\mathrm{had}}$: the p_{T} of the hadronic top-quark in a single-lepton event.
- $p_{\mathrm{T}}^{t\bar{t}}$: the p_{T} of the reconstructed top-quark pair system.
- $|y^{t\bar{t}}|$: the y of the reconstructed top-quark pair system.
- $m^{t\bar{t}}$: the mass of the reconstructed top-quark pair system.
- $|\Delta\phi(t,\bar{t})|$: the angular distance in ϕ between the two reconstructed top-quarks.
- $H_{\mathrm{T}}^{t\bar{t}}$: the scalar sum of the p_{T} of the two reconstructed top-quarks.
- $\chi^{t\bar{t}}$: the exponential of the absolute difference of leading and sub-leading top-quark rapidities ($\exp(|y^{t,1} - y^{t,2}|)$.
- N_{jets}: the number of jets.
- $N^{\mathrm{extra-jets}}$: the number of additional jets after considering the jets used to reconstruct the top-quark pair.
- $R_{\mathrm{jet1}}^{\mathrm{extra1}}$: the ratio of the leading additional jet p_{T} to the leading jet p_{T}.
- $R_{\mathrm{extra1}}^{t\bar{t}}$: the ratio of the $p_{\mathrm{T}}^{t\bar{t}}$ to the p_{T} of the leading additional jet.
- $\Delta R_{\mathrm{jet1}}^{\mathrm{extra1}}$: the ΔR between the leading additional jet and the leading jet.
- $\Delta R_{t,\mathrm{close}}^{\mathrm{extra1}}$: the ΔR between the leading additional jet and the closest top-quark.
- Lepton p_{T}: the p_{T} of both leptons in a dilepton event.
- $p_{\mathrm{T}}{}^{e\mu}$: the p_{T} of the dilepton system.
- $p_{\mathrm{T}}{}^{e}$+$p_{\mathrm{T}}{}^{\mu}$: the sum of p_{T} of the two leptons.
- $\mathrm{m}^{e\mu}$: the mass of the dilepton system.

6 NLO+PS Matching algorithm uncertainty

The matching algorithm uncertainty is defined to cover the difference between algorithmic approaches to perform the NLO+PS matching, in particular between the POWHEG [6–9] and the MC@NLO [54] methods. This uncertainty should not affect the decay products of the top-quark and should be relevant only for variables sensitive to $t\bar{t}$ production as the $p_{\mathrm{T}}^{t,had}$ or $p_{\mathrm{T}}^{t\bar{t}}$. This uncertainty is among the dominant ones for several measurements that include the $t\bar{t}$ process as the main signal or background [49, 55, 56].

The procedure predominantly employed by Run-2 analyses to evaluate the NLO+PS matching algorithm uncertainty compares the nominal POWHEG+PYTHIA 8 sample with MG5_aMC@NLO+PYTHIA 8*, and is referred to as ME(PY) in the following sections. For these comparisons both the predictions are taken with the recommended list of showering parameters, depending on the matching algorithm employed. Moreover some of the PYTHIA 8 parameters have been tuned from ATLAS using $t\bar{t}$ Z-boson and jets measurements in [13]. Figure 1 shows several predictions for the invariant mass of the lepton and b-jet in the ℓ+jets channel, which should only be affected by the top-quark decay products kinematics; it is clear that the difference between POWHEG+PYTHIA 8 and MG5_aMC@NLO+PYTHIA 8* affects the decay products too.

These two samples have several differences in the shower settings, listed in Table 2. The motivation for several of these differences is in the different NLO+PS matching algorithm, that requires different showering settings to avoid any double counting in the radiation when matching the hard scatter and the parton shower predictions. These differences have an impact also on the top-quark decay product kinematics, which should not be sensitive to the matching algorithm itself. This is shown in Figure 1, where the two predictions are compared for the invariant mass of the lepton and b-jet in the ℓ+jets channel (m_{lb}). The effect of the different settings in the PYTHIA8 is that ME(PY) convolutes two effects: the NLO+PS matching procedure and the different settings. To try to mitigate the overlap of different effects, a new PYTHIA8 has been generated with `TimeShower:MEcorrections` set to off. This reduces the accuracy of the top-quark decay to LO, while leaving the NLO accuracy of the $t\bar{t}$ production unaffected. This setting cannot be turned on in MADGRAPH5_aMC@NLO+PYTHIA 8 without introducing an inconsistency with the MC subtraction term. This change greatly improves the agreement of the two samples on M_{lb}, as shown by the comparison of MG5_aMC@NLO+PYTHIA 8* and PWG+PY8(MEC off) in Figure 1.

The difference between the new sample and MG5_aMC@NLO+PYTHIA 8* can be taken as an uncertainty which is applied to the nominal sample and is termed ME(PY*) in the following. Ideally the NLO+PS matching algorithm uncertainty should be independent of the choice of parton shower as additional uncertainties can cover the choice of the shower settings separately. To verify that the new uncertainty ME(PY*) is independent from the showering choice, a new definition of the NLO+PS matching algorithm uncertainty is considered in which the HERWIG7.1.3 parton shower replaces PYTHIA8. Specifically, HERWIG7.1.3 was interfaced with both POWHEG and MADGRAPH5_aMC@NLO, keeping similar showering parameters, as the matrix element corrections that is enabled in both. The remaining differences related to the matching procedure between the two samples are shown in Table 3. The uncertainty evaluated by comparing these two predictions will be referred to as ME(H7). By comparing the ME(PY*) and ME(H7) uncertainties it should be possible to understand if the new definition of the uncertainty covers only the difference between the NLO+PS matching algorithm or still contains some dependency on the showering.

The NLO+PS matching algorithm uncertainties evaluated with the three approaches described above are shown in Figure 2-8. The upper section of each figure shows the comparison among the various

Pythia8 settings	in MadGraph5_aMC@NLO+Pythia 8	in Powheg+Pythia 8
SpaceShower:rapidityOrder	on	on
SigmaProcess:alphaSvalue	0.14	0.14
SpaceShower:pT0Ref	1.56	1.56
SpaceShower:pTmaxFudge	1	0.91
SpaceShower:pTdampFudge	1.05	1.05
SpaceShower:alphaSvalue	0.127	0.127
TimeShower:alphaSvalue	0.127	0.127
BeamRemnants:primordialKThard	1.88	1.88
MultipartonInteractions:pT0Ref	2.09	2.09
MultipartonInteractions:alphaSvalue	0.126	0.126
SpaceShower:MEcorrections	off	on
TimeShower:pTmaxMatch	1	2
TimeShower:pTmaxFudge	1	1
TimeShower:MEcorrections	off	on
TimeShower:globalRecoil	on	off
TimeShower:limitPTmaxGlobal	on	off
TimeShower:nMaxGlobalRecoil	1	1
TimeShower:globalRecoilMode	2	0
TimeShower:nMaxGlobalBranch	1	-1
TimeShower:weightGluonToQuark	1	4

Table 2: Detailed settings used in the matching of Pythia 8 to MadGraph5_aMC@NLO and Powheg. Settings that differ between the two generators are shown in red, while those that are identical are shown in black.

Herwig7.1 settings	in MadGraph5_aMC@NLO
KinematicsReconstructor:ReconstructionOption	General
KinematicsReconstructor:InitialInitialBoostOption	LongTransBoost
KinematicsReconstructor:InitialStateReconOption	Rapidity
KinematicsReconstructor:FinalStateReconOption	Default
ShowerHandler:SpinCorrelations	No

Table 3: Special settings used in the matching of Herwig7.1.3 to MadGraph5_aMC@NLO, that differs from the matching to Powheg settings.

particle-level predictions to the unfolded data, reported with their experimental uncertainty band. This illustrates that all the predictions employed are in reasonable agreement with the data and can be used to estimate the NLO+PS matching algorithm uncertainty. The bottom section of each figure shows the $t\bar{t}$ production cross-section for the nominal Powheg+Pythia 8 sample with three different uncertainty bands, depending on the NLO+PS matching algorithm uncertainty approach employed. The uncertainties are evaluated as the difference on the particle-level distributions, reported as relative difference to the nominal prediction from Powheg+Pythia 8 and symmetrized.

Figures 2 and 3 show the three NLO+PS matching algorithm uncertainty approaches on the observables $p_{\mathrm{T}}^{t,1}$ (normalised) and $p_{\mathrm{T}}^{t\bar{t}}$ (absolute). In the ℓ+jets channel, the largest uncertainty on the majority of the bins is obtained with ME(PY) and reaches 10% and 37% in the tails of the $p_{\mathrm{T}}^{t,1}$ and $p_{\mathrm{T}}^{t\bar{t}}$ distributions, respectively. The ME(PY*) and ME(H7) approaches lead to smaller uncertainties in general, but differences are seen between them. In the $p_{\mathrm{T}}^{t\bar{t}}$ distribution of the ℓ+jets channel this difference is of order 10% near 200 GeV and in the $p_{\mathrm{T}}^{t,1}$ distribution it is $\approx$ 5% between 350 and 500 GeV. While the picture in the all-hadronic channel is similar for the absolute distributions, where ME(PY) is the dominant uncertainty in all bins, the

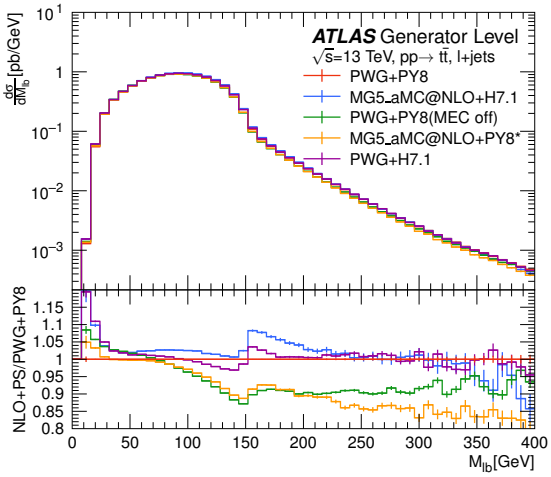

Figure 1: Differential $t\bar{t}$ production cross-section as a function of the invariant mass of the system formed by the lepton and the b-jet used to reconstruct the leptonic top-quark with the pseudo-top algorithm in the ℓ+jets channel. The bottom pad shows the ratio of all NLO+PS predictions to the nominal Powheg+Pythia 8 prediction.

situation is different for the normalised $p_{\mathrm{T}}^{t,1}$ distribution. Here, the uncertainty obtained with ME(PY*) and ME(H7) are similar on the whole distribution, with the largest difference being around 3%, whereas ME(PY) leads to an uncertainty below 1% everywhere. Figure 4 shows the $|y^{t\bar{t}}|$ distribution for the ℓ+jets and all-hadronic channels. The uncertainty is flat along the full distribution for all three approaches, with ME(PY) being the largest overall.

Figure 5 shows variables in the all-hadronic channel which are particularly sensitive to the kinematics of the leading extra radiation. The three approaches to estimate the uncertainty lead to different results. The largest differences between ME(PY*) and ME(H7) is observed in the first bin of the $R_{\mathrm{extra1}}^{p_{\mathrm{T}},t\bar{t}}$ distribution, where the uncertainty is 3% and 7%, respectively, and in the second and third bins of the $R_{\mathrm{jet1}}^{p_{\mathrm{T}},\mathrm{extra1}}$ distribution, where ME(PY*) and ME(H7) are $\approx$ 7% and 3%, respectively. The ME(PY) uncertainty differs from both ME(PY*) and ME(H7), and reaches $\approx$ 12% in the tail of the $\Delta R_{\mathrm{t,close}}^{\mathrm{extra1}}$ distribution while ME(PY*) and ME(H7) are $\approx$ 2%. None of the three uncertainty definitions is dominant in all bins of the three observables.

Figure 6 shows kinematic variables of the lepton and dilepton system, produced by the decay of the top-quark pair. In the p_{T} distributions the NLO+PS matching algorithm uncertainty increases significantly in the high p_{T} region (above 100 GeV) for all three approaches, with the ME(PY) being the largest. The ME(H7) and ME(PY*) approaches lead to similar sized uncertainties on a large fraction of the spectra, but differ in the higher p_{T} tails. In the $m^{e\mu}$ spectra the three approaches lead to a similar sized uncertainty.

Figure 7 shows variables of the $t\bar{t}$ system sensitive to the kinematics of both the top and anti-top quarks of the events in the ℓ+jets channel. For these observables, the ME(PY) approach leads to the largest uncertainty, with ME(PY) and ME(PY*) being similarly sized on $m^{t\bar{t}}$, though these two approaches lead to different uncertainties on $\Delta\Phi(t\bar{t})$ and $H_{\mathrm{T}}^{t\bar{t}}$. For $H_{\mathrm{T}}^{t\bar{t}}$ the uncertainties around 600 GeV are $\approx$ 8%, 5% and <1% for ME(PY8), ME(PY8*) and ME(H7), respectively.

Figure 8 shows the $t\bar{t}$ production as a function of the number of jets in the all-hadronic channel and the number of extra jets not used to reconstruct the $t\bar{t}$ system in the ℓ+jets channel. It can be seen that for these

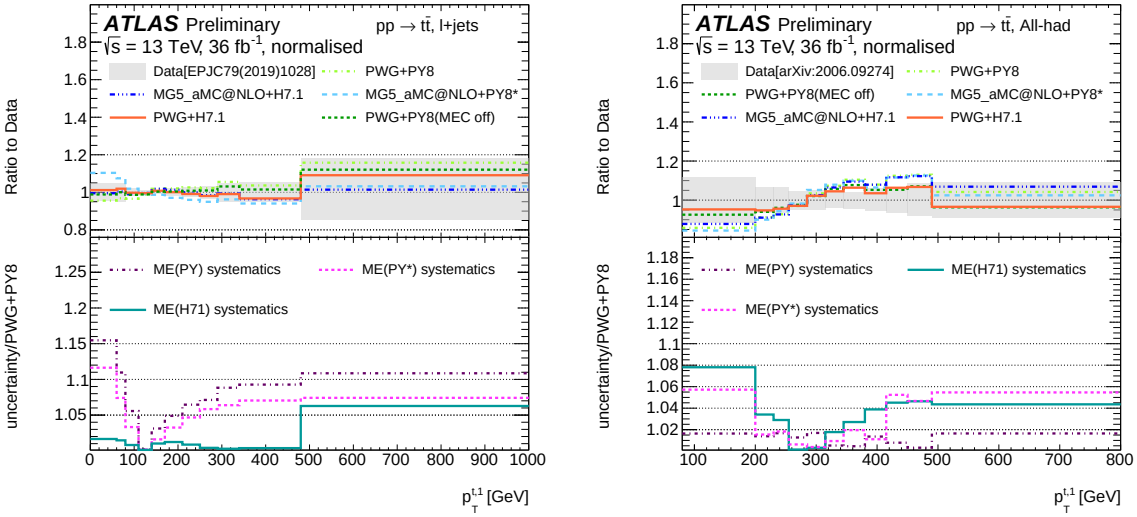

Figure 2: Differential $t\bar{t}$ production cross-section as a function of $p_{\mathrm{T}}^{t,1}$ in the ℓ+jets channel [49] (left) and in the all-hadronic channel [53]. The uncertainty bands are defined as the difference of the particle-level prediction between two samples, one obtained with POWHEG and the other with MADGRAPH5_aMC@NLO. The three different bands correspond to different showering algorithms interfaced with the hard scatter generators. The top panel shows the ratio of each sample to data, including the measurement uncertainty. The bottom panel shows the ratio of each uncertainty band to the nominal POWHEG+PYTHIA 8, since the uncertainty band is defined to be symmetric, only one side of the uncertainty is shown.

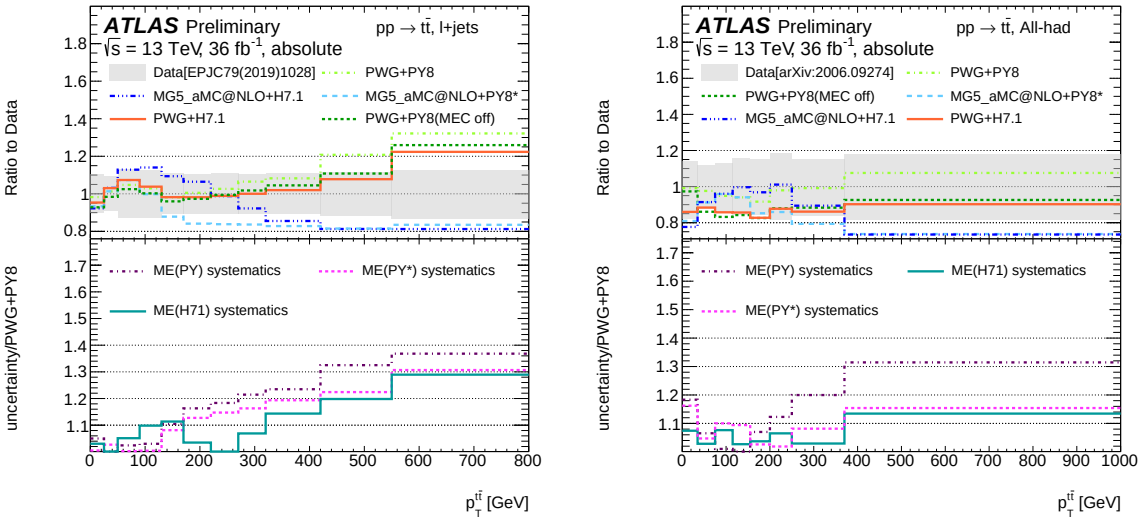

Figure 3: Differential $t\bar{t}$ production cross-section as a function of $p_{\mathrm{T}}^{t\bar{t}}$ in the ℓ+jets channel [49] (left) and in the all-hadronic channel [53]. The uncertainty bands are defined as the difference of the particle-level prediction between two samples, one obtained with POWHEG and the other with MADGRAPH5_aMC@NLO. The three different bands correspond to different showering algorithms interfaced with the hard scatter generators. The top panel shows the ratio of each sample to data, including the measurement uncertainty. The bottom panel shows the ratio of each uncertainty band to the nominal POWHEG+PYTHIA 8, since the uncertainty band is defined to be symmetric, only one side of the uncertainty is shown.

observables, ME(PY) leads to the largest uncertainty for most of the distributions, while ME(H7) is the largest uncertainty on the cross-section for $t\bar{t}$ production with exactly one extra jet.

In a large set of kinematic observables in the three channels, especially for the absolute distributions, ME(PY) gives more conservative uncertainties than both ME(H71) and ME(PY*). This indicates that the attempt to use coherent shower settings reduces the NLO+PS matching algorithm uncertainty. However, differences between ME(PY*) and ME(H7) shapes are visible in all the distributions and can become significant in many observables. This suggests that there are parameters in the showering algorithm that are still different in the matching to POWHEG and MADGRAPH5_aMC@NLO and hence the estimates of the NLO+PS matching algorithm uncertainty may probe additional parton-shower effects in addition to the pure algorithmic differences. These differences are related to the approach used for the matching and is not possible to completely disentangle between the showering setting and the matching algorithm.

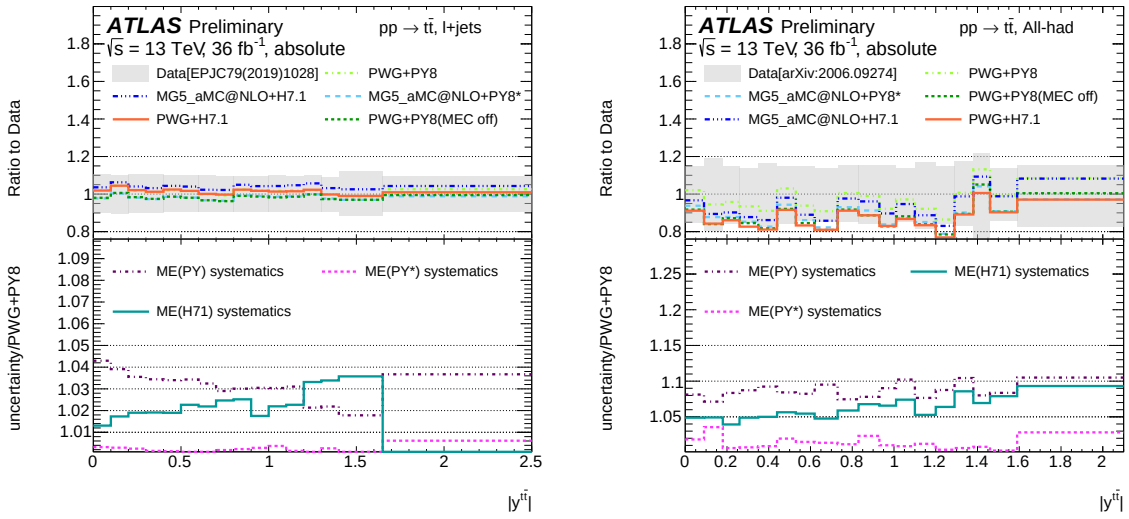

Figure 4: Differential $t\bar{t}$ production cross-section as a function of $y^{t\bar{t}}$ in the ℓ+jets channel [49] (left) and in the all-hadronic channel [53] (right). The uncertainty bands are defined as the difference of the particle-level prediction between two samples, one obtained with POWHEG and the other with MADGRAPH5_aMC@NLO. The three different bands correspond to different showering algorithms interfaced with the hard scatter generators. The top panel shows the ratio of each sample to data, including the measurement uncertainty. The bottom panel shows the ratio of each uncertainty band to the nominal POWHEG+PYTHIA 8, since the uncertainty band is defined to be symmetric, only one side of the uncertainty is shown.

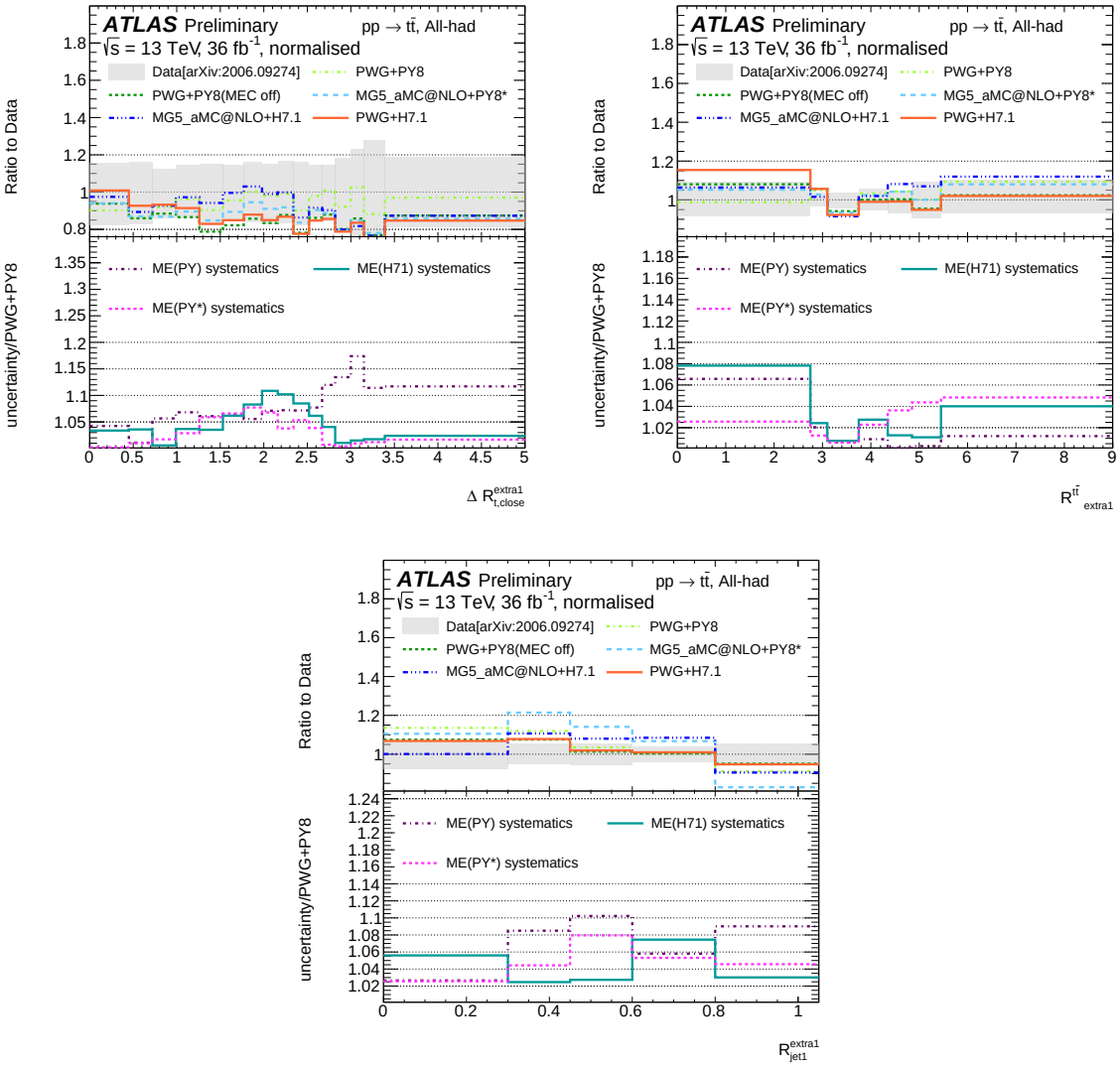

Figure 5: Normalised differential $t\bar{t}$ production cross-section as a function of the ΔR between the leading additional jet and the closest top-quark (top left), the ratio of the $p_{\mathrm{T}}^{t\bar{t}}$ to the p_{T} of the leading additional jet (top right) and the ratio of the leading additional jet p_{T} to the leading jet p_{T} (bottom). The uncertainty bands are defined as the difference of the particle-level prediction between two samples, one obtained with POWHEG and the other with MADGRAPH5_aMC@NLO. The three different bands correspond to different showering algorithms interfaced with the hard scatter generators. The top panel shows the ratio of each sample to data, including the measurement uncertainty. The bottom panel shows the ratio of each uncertainty band to the nominal POWHEG+PYTHIA 8, since the uncertainty band is defined to be symmetric, only one side of the uncertainty is shown. The comparison is performed in all-hadronic channel, detailed in [53].

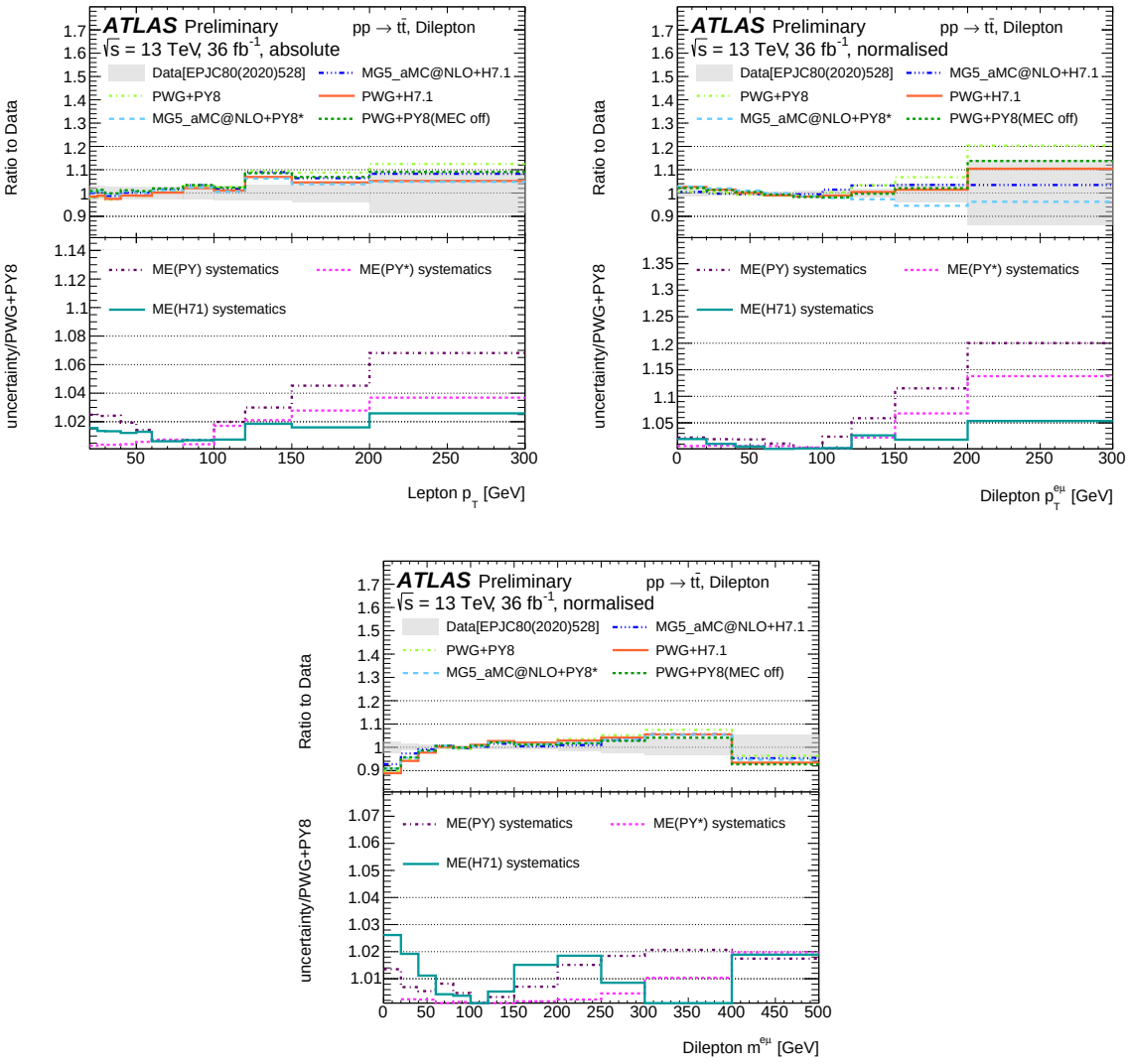

Figure 6: Absolute differential $t\bar{t}$ production cross-section as a function of the lepton p_{T} (top left), dilepton $p_{\mathrm{T}}^{e\mu}$ (top right) and dilepton $m^{e\mu}$ (bottom). The uncertainty bands are defined as the difference of the particle-level prediction between two samples, one obtained with POWHEG and the other with MADGRAPH5_aMC@NLO. The three different bands correspond to different showering algorithms interfaced with the hard scatter generators. The top panel shows the ratio of each sample to data, including the measurement uncertainty.The bottom panel shows the ratio of each uncertainty band to the nominal POWHEG+PYTHIA 8, since the uncertainty band is defined to be symmetric, only one side of the uncertainty is shown. The comparison is performed in the dilepton channel, detailed in [52].

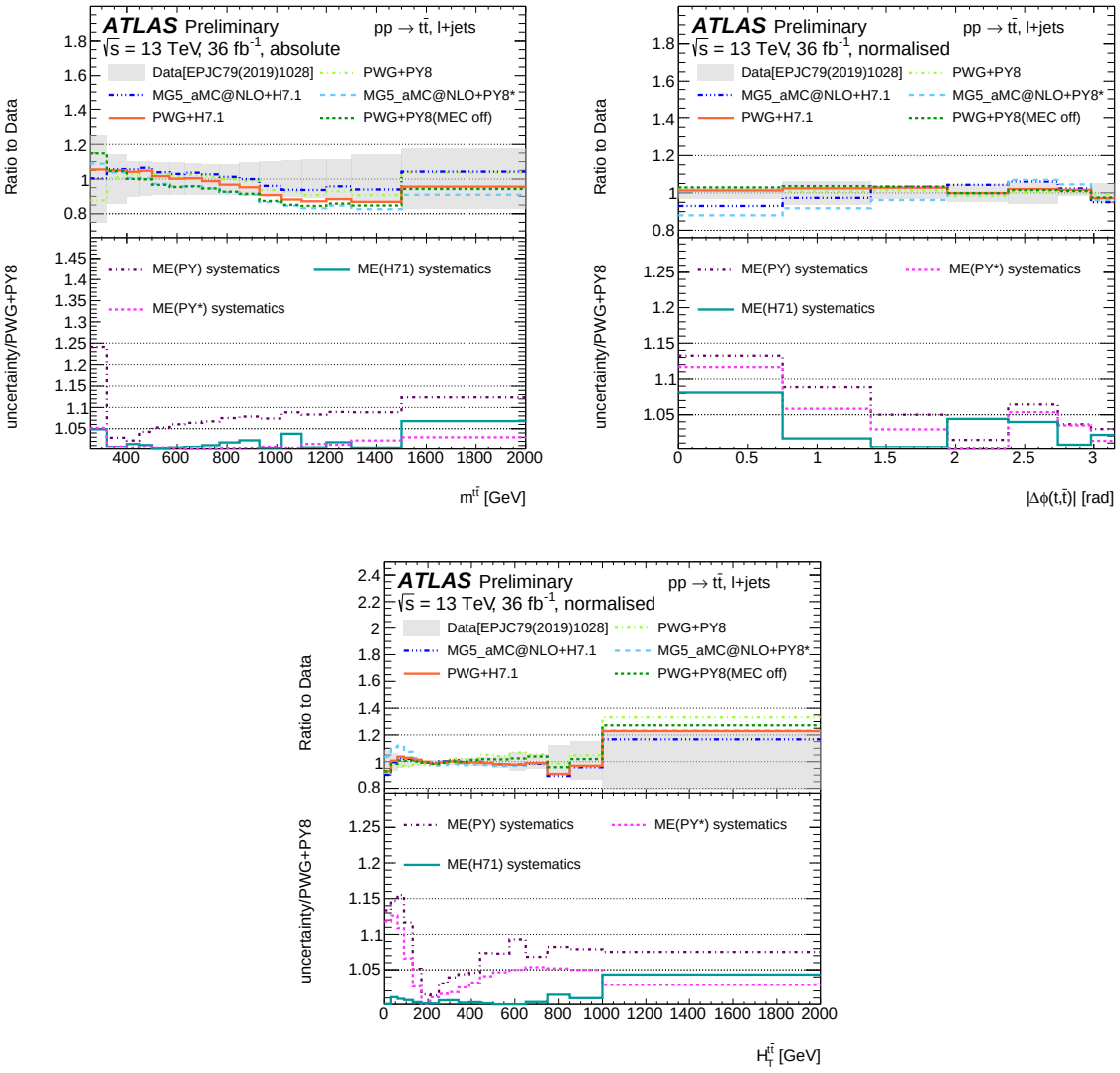

Figure 7: Differential $t\bar{t}$ production cross-section as a function of the $m^{t\bar{t}}$(top left), $\Delta\phi(t\bar{t})$ (top right) and $H_{\mathrm{T}}^{t\bar{t}}$(bottom). The top left reports the comparison of absolute spectra while the top right and the bottom show normalised spectra. The uncertainty bands are defined as the difference of the particle-level prediction between two samples, one obtained with POWHEG and the other with MADGRAPH5_aMC@NLO. The three different bands correspond to different showering algorithms interfaced with the hard scatter generators. The top panel shows the ratio of each sample to data, including the measurement uncertainty. The bottom panel shows the ratio of each uncertainty band to the nominal POWHEG+PYTHIA 8, since the uncertainty band is defined to be symmetric, only one side of the uncertainty is shown. The comparison is performed in a ℓ+jets channel, detailed in [49].

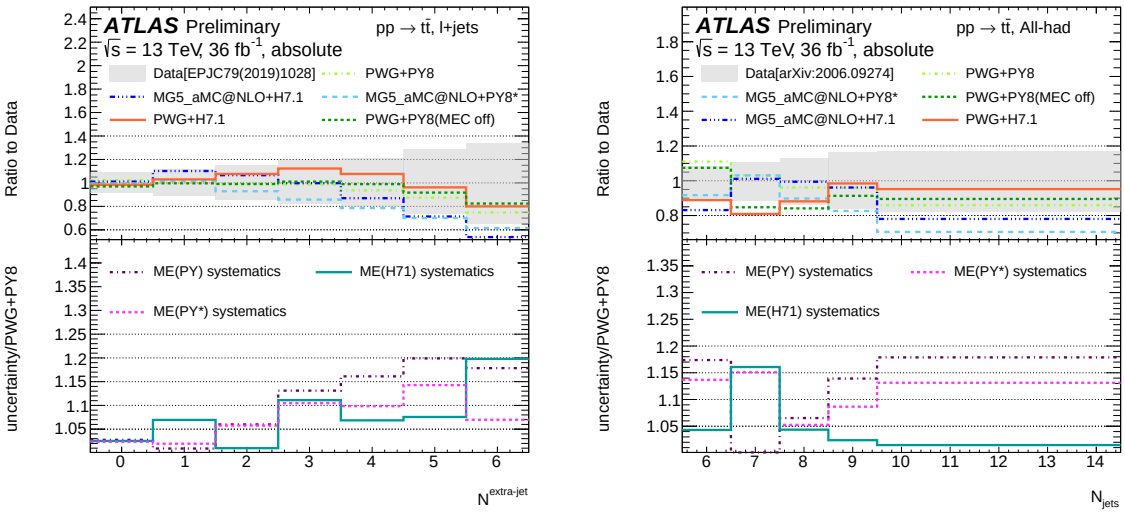

Figure 8: Absolute differential $t\bar{t}$ production cross-section as a function of the number of extra-jets in the l+jets channel [49] (left) and of the number of jets in the all-hadronic channel [53] (right). The uncertainty bands are defined as the difference of the particle-level prediction between two samples, one obtained with POWHEG and the other with MADGRAPH5_aMC@NLO. The three different bands correspond to different showering algorithms interfaced with the hard scatter generators. The top panel shows the ratio of each sample to data, including the measurement uncertainty. The bottom panel shows the ratio of each uncertainty band to the nominal POWHEG+PYTHIA 8, since the uncertainty band is defined to be symmetric, only one side of the uncertainty is shown.

7 Parton-shower uncertainty

The approach typically used throughout Run-2 to evaluate the parton-shower uncertainty is based on comparing the nominal POWHEG +PYTHIA8 sample to the POWHEG +HERWIG7.0.4, which is referred to as PS(H7.0) in the following. Here we compare this approach with an alternative approach based on a comparison to an updated version of POWHEG +HERWIG7.1.3. The difference between the nominal POWHEG +PYTHIA8 sample and the POWHEG +HERWIG7.1.3 sample is referred to as PS(H7.1). The differences between the two versions of HERWIG7 are described in Section 2. The effect of these differences on the variables shown in this note is expected to be small.

In Figure 9, the parton shower uncertainties evaluated with the two approaches described above are shown. Each figure consists of two panels; the top panel shows the ratio of each sample to data and the uncertainty associated to the data. The bottom panel shows the size of the uncertainties from the different strategies. The uncertainties are evaluated as the difference of the particle-level distributions between the samples described above, reported as relative difference to the nominal POWHEG+PYTHIA 8. The uncertainty band is symmetrized around the nominal. POWHEG +HERWIG7.0.4 and POWHEG +HERWIG7.1.3 are in similar agreement with the data, with the newest version showing a slight improvement of a few percent in the agreement with the data on all distributions shown in Figure 9. Both these predictions provide a qualitatively better description of the data than POWHEG+PYTHIA 8. Depending on the decay channel and the observable, the parton shower uncertainty slightly increases (decreases) if POWHEG +HERWIG7.1.3 is further away from (more similar to) POWHEG+PYTHIA 8 then POWHEG +HERWIG7.0.4.

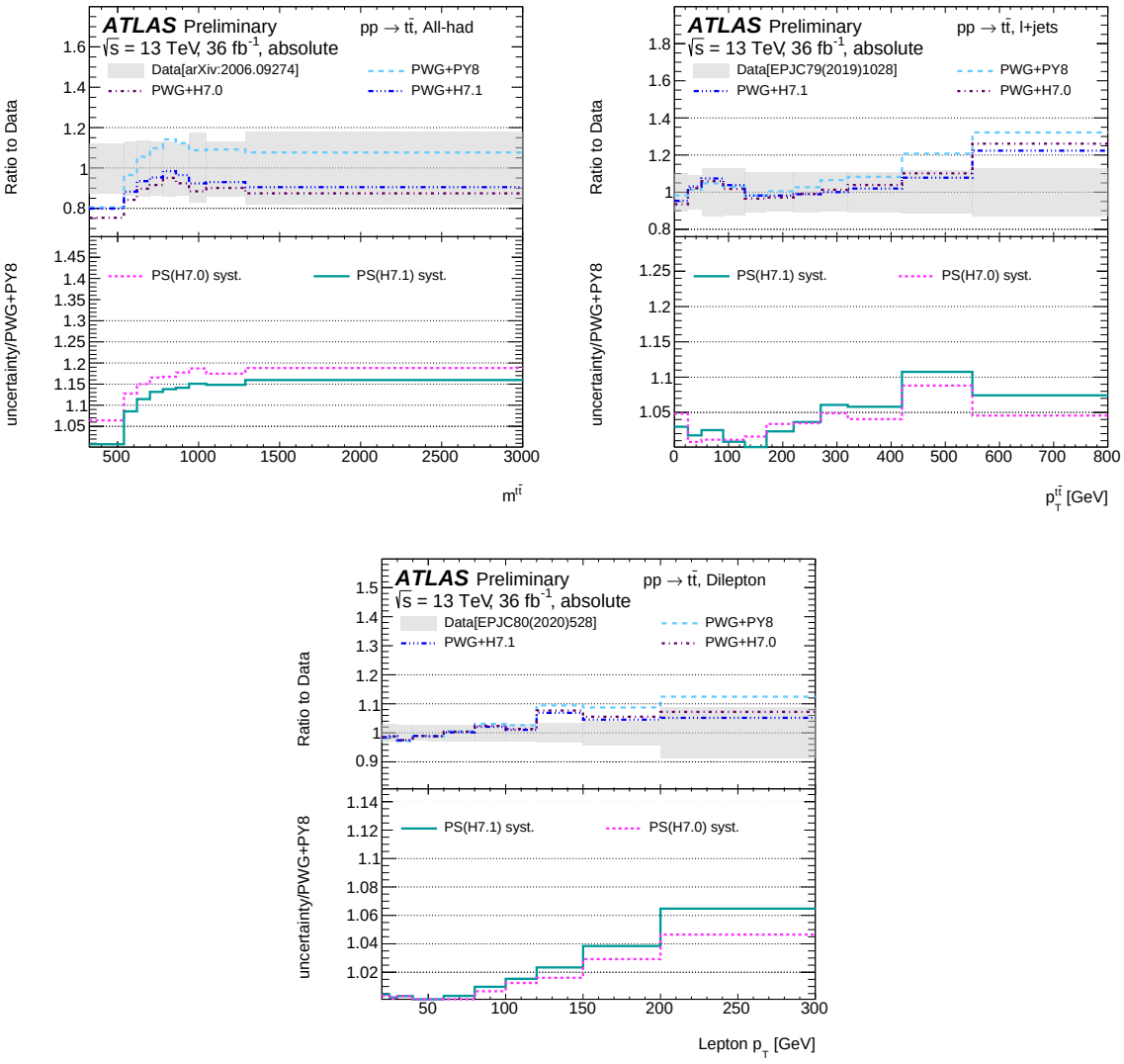

Figure 9: Differential cross-section for $t\bar{t}$ production as a function of $m_{t\bar{t}}$ in the all-hadronic channel [53] (top left), $p_{\mathrm{T}}^{t\bar{t}}$ in the l+jets channel [49] (top right) and lepton p_{T} in the dilepton channel [52] (bottom). The top panel shows the ratio of each sample to data, including the measurement uncertainty. The bottom panel shows the ratio of each uncertainty to the nominal Powheg+Pythia 8, since the uncertainty band is defined to be symmetric, only one side of the uncertainty is shown.

8 Uncertainties due to initial-state radiation

The approach typically used by Run-2 analyses on ATLAS to asses the uncertainty related to the initial state radiation (ISR), introduced in Section 3, requires the comparison of the nominal POWHEG+PYTHIA8 sample to two alternative samples using different settings of h_{damp}, the normalisation and factorisation scales in the hard scatter, as well as showering scales. The showering scales are varied according to the Var3c eigentunes of the A14 showering tune. The variations of the uncertainty, derived as mentioned in Section 3, was seen to sufficiently bracket the difference between the nominal prediction and the measured data for variables such as the number of additional jets and $p_{\text{T}}^{t\bar{t}}$, measured at 8 TeV [3]. Because of the new measurements performed at 13 TeV, it is now possible to re-evaluate the definition of this uncertainty.

The uncertainties are primarily split in scale variations and alternative h_{damp} parameters, then the effect of correlating the scale variations in the hard scatter with the variations of the A14 tune is studied in detail. This last study on the correlations is performed following previous theoretical studies [57] that indicate correlating these scales is a more correct approach.

8.1 h_{damp} uncertainty

The h_{damp} value used in the nominal POWHEG+PYTHIA8 sample is set to 1.5 m_{top}. The uncertainty on this parameter can be evaluated by varying it by a factor of 0.5 and 2.0. For simplicity, only one variation of h_{damp} is considered in the current ATLAS uncertainty prescription corresponding to a factor of two increase with respect to the nominal value; the uncertainty obtained is then symmetrised. The following study explores how this prescription differs from producing individual samples which vary h_{damp} by a factor 2.0 and 0.5.

In the top pad of Figures 10-12, three predictions with different values of h_{damp} (0.75, the nominal 1.5 and 3.0 times the mass of the top-quark) are compared to the data. In the bottom pad, the h_{damp}=0.75 m_{top} sample is compared to the uncertainty band obtained by symmetrising the differences between the samples generated with h_{damp}=1.5 m_{top} and h_{damp}=3.0 m_{top}.

The comparison with the data shows that the two variations of h_{damp} bracket the nominal value of h_{damp}=1.5 m_{top}, with the data showing a slight preference toward lower values of h_{damp} in the tails of the distributions, especially in the dilepton and ℓ+jets phase space shown in Figures 12 and Figures 11 (right). In the all-hadronic phase-space the results are different; h_{damp}=0.75 m_{top} predicts a very low fiducial cross-section, shown in Figure 10, resulting in a large difference with the data in all the absolute distributions. Moreover, the shapes predicted with a lower h_{damp} value are worse than with h_{damp}=3.0 m_{top}.The differences between the all-hadronic and the other channels could be related to the different fiducial selection, that in the all-hadronic channel requires at least 6 jets with p_{T} above 55 GeV, while only 4 jets at 25 GeVand no jets in the ℓ+jets and dileptonic channel, respectively.

Concerning the use of the h_{damp}=0.75 m_{top} sample as a downward h_{damp} variation, the figures show that for the majority of the observables studied, the new variation would lead to a similar uncertainty to the one obtained by symmetrising the uncertainty obtained comparing h_{damp}=1.5 m_{top} and h_{damp}=3.0 m_{top}. However, in some observables, such as Figure 10 (right) and Figure 11 (right), using h_{damp}=0.75 m_{top} would result in a significantly larger uncertainty. The agreement with the data is reasonable for h_{damp}=0.75 m_{top} and h_{damp}=3.0 m_{top}, and the largest differences are observed in the all-hadronic phase-space where

h_{damp}=0.75 m_{top} provide a very poor description of the data, which indicates that the symmetrized approach is a valid method to estimate the h_{damp} uncertainty.

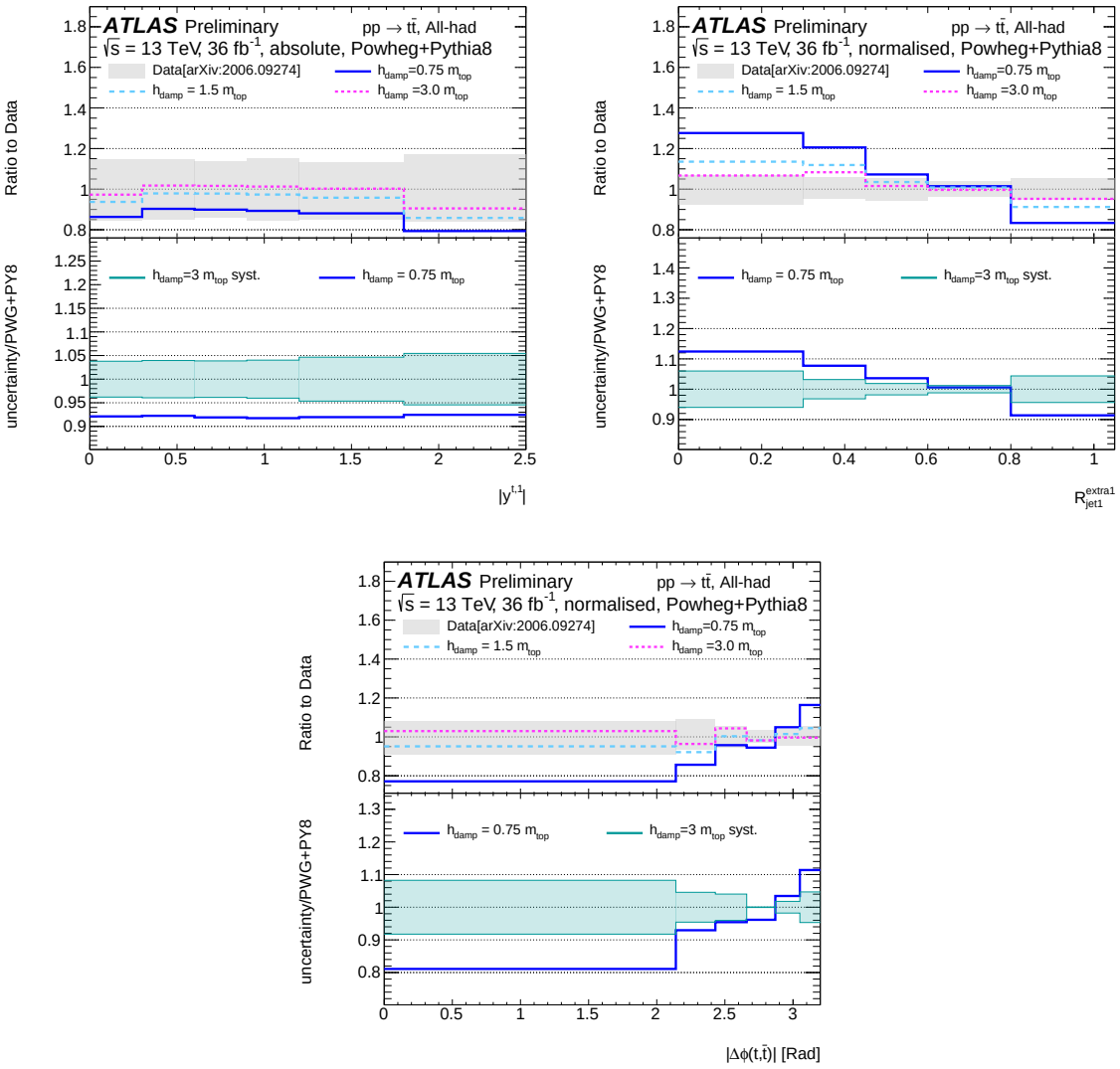

Figure 10: Differential $t\bar{t}$ production cross-section as a function of $|y^{t,1}|$ (top left), the ratio of the leading additional jet p_{T} to the leading jet p_{T} (top right), $\Delta\phi(t\bar{t})$ (bottom). All the distributions are normalised. In the top panel, the three different Powheg+Pythia 8 h_{damp} predictions (0.75 m_{top}, 1.5 m_{top} and 3.0 m_{top}) are compared to the unfolded data. The uncertainty bands on these predictions are statistical only. In the bottom panel, the uncertainty bands reflect the symmetrised difference at particle-level between the Powheg+Pythia 8 sample obtained with h_{damp}=3 m_{top} and the nominal Powheg+Pythia 8, with h_{damp}=1.5 m_{top}. The band is compared to Powheg+Pythia 8 with h_{damp} set to 0.75 m_{top}, this distribution contains the statistical uncertainty of the sample. The comparison is performed in the all-hadronic channel [53].

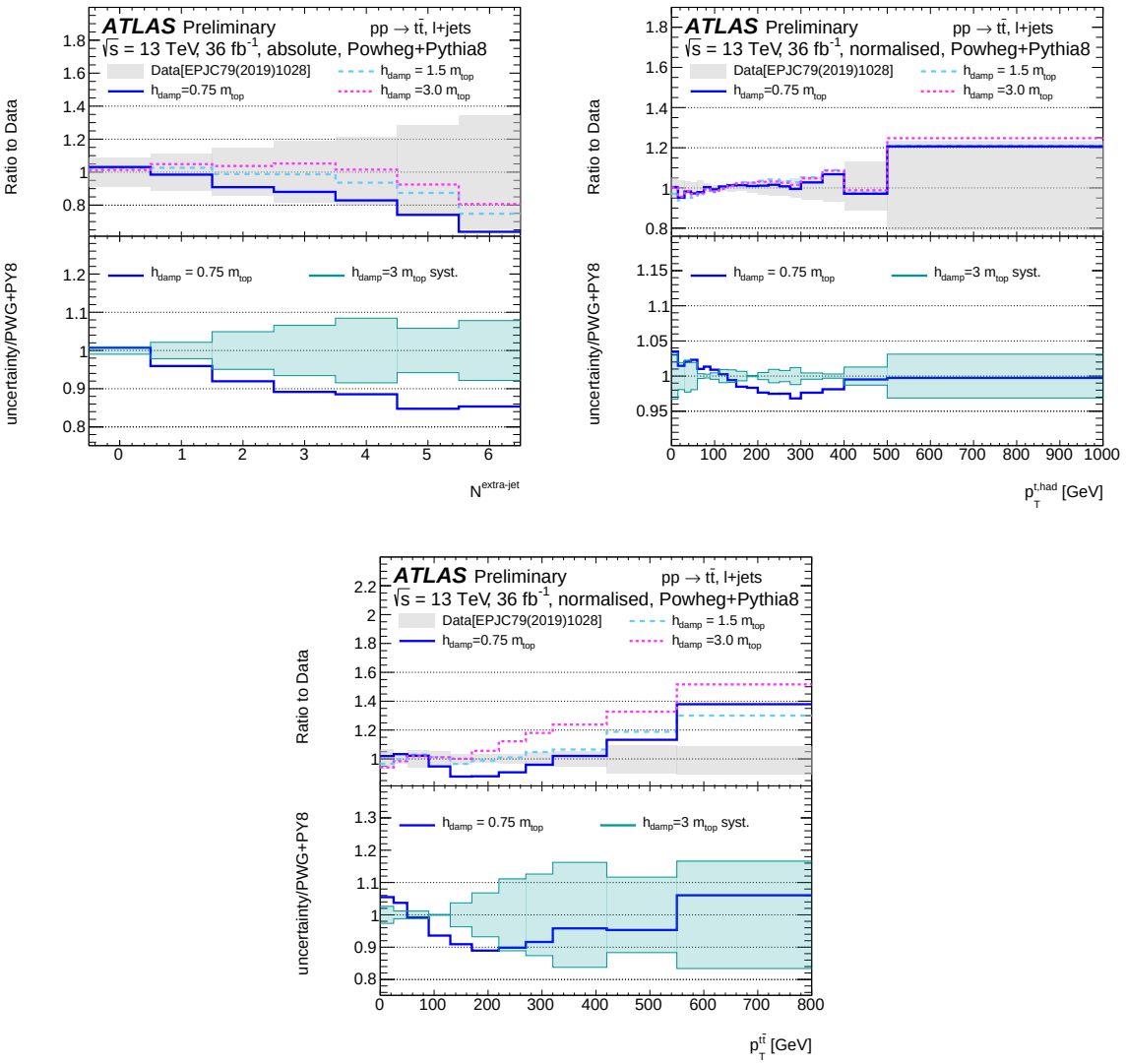

Figure 11: Differential $t\bar{t}$ production cross-section as a function of $N^{\text{extra-jet}}$ (top left), $p_{\text{T}}^{t,\text{had}}$ (top right) and $p_{\text{T}}^{t\bar{t}}$ (bottom). The top left distribution shows the absolute cross-section, while the normalised cross-section is shown in the other distributions. In the top panel, the three different Powheg+Pythia 8 h_{damp} predictions (0.75 m_{top}, 1.5 m_{top} and 3.0 m_{top}) are compared to the unfolded data. The uncertainty bands on these predictions are statistical only. In the bottom panel, the uncertainty bands reflect the symmetrised difference at particle-level between the Powheg+Pythia 8 sample obtained with h_{damp}=3 m_{top} and the nominal Powheg+Pythia 8, with h_{damp}=1.5 m_{top}. The band is compared to Powheg+Pythia 8 with h_{damp} set to 0.75 m_{top}, this distribution contains the statistical uncertainty of the sample. The comparison is performed in the ℓ+jets channel [49].

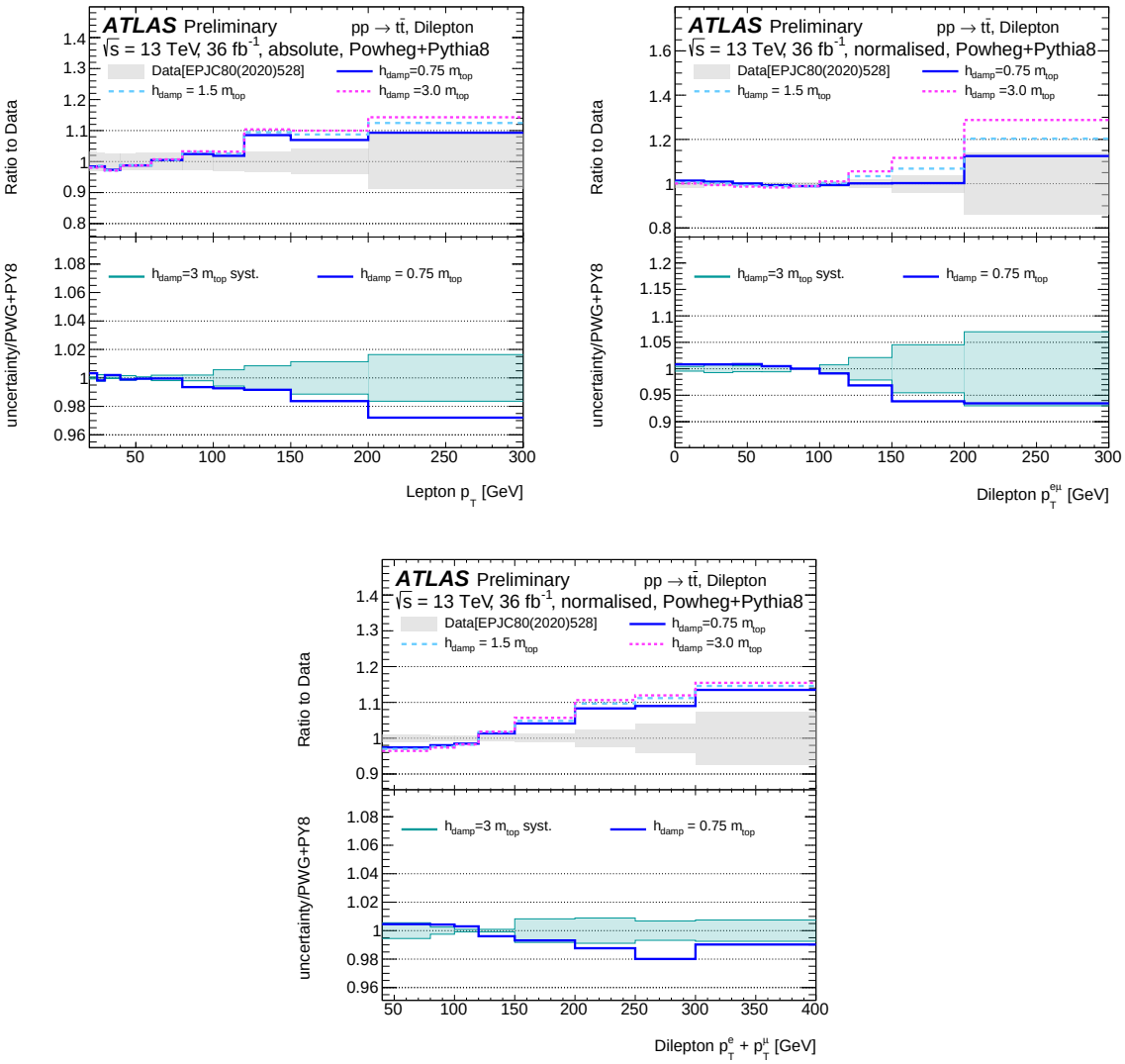

Figure 12: Differential $t\bar{t}$ production cross-section as a function of lepton p_{T} (top left), dilepton $p_{\mathrm{T}}^{e\mu}$ (top right) and dilepton $E^{e} + E^{\mu}$ (bottom). The top left distribution shows the absolute cross-section, while the normalised cross-section is shown in the other cases. In the top panel, the three different Powheg+Pythia 8 h_{damp} predictions (0.75 m_{top}, 1.5 m_{top} and 3.0 m_{top}) are compared to the unfolded data. The uncertainty bands on these predictions are statistical only. In the bottom panel, the uncertainty bands reflect the symmetrised difference at particle-level between the Powheg+Pythia 8 sample obtained with h_{damp}=3 m_{top} and the nominal Powheg+Pythia 8, with h_{damp}=1.5 m_{top}. The band is compared to Powheg+Pythia 8 with h_{damp} set to 0.75 m_{top}, this distribution contains the statistical uncertainty of the sample. The comparison is performed in the dilepton channel [52].

8.2 Scale variations

The samples used to study the effect of correlating or decorrelating the scale variation between ME and PS are shown in Figures 13–15. In the top panel, three samples are compared to the data. They are the nominal sample and the *Scale Corr. Down(Up)* predictions which are obtained by correlating the hard scatter scale variation μ_R=0.5(2.0) and μ_F=0.5(2.0) with the Var3cUp(Down) variation of the A14 tune. The Var3cUp(Down) variations correspond to changing the PYTHIA 8 parameter *SpaceShower:alphaSvalue* in the range [0.140,0.115], with respect to the nominal value of 0.127. In terms of scale variations this corresponds to the range μ_R^{ISR}=[0.55,1.96]. The bottom panel compares the scale uncertainty obtained with different assumptions on the correlations between the scale uncertainties in the hard scatter and the A14 variations in the showering. The uncertainty defined as *Scale Uncorr.* is obtained by summing in quadrature the envelope of the 7-point hard-scattering scale variations obtained by varying independently μ_R and μ_F by a factor 2.0 and 0.5 with the uncertainty obtained as the envelope between the Var3cUp and Var3cDown variations of the A14 tune.

The correlated variations tend to give a smaller uncertainty band at low $p_{\mathrm{T}}^{t,\mathrm{had}}$, high $N^{\text{extra-jet}}$, shown in Figure 14, and in lepton p_{T}, shown in Figure 15, but in general there is a small difference between the two approaches.

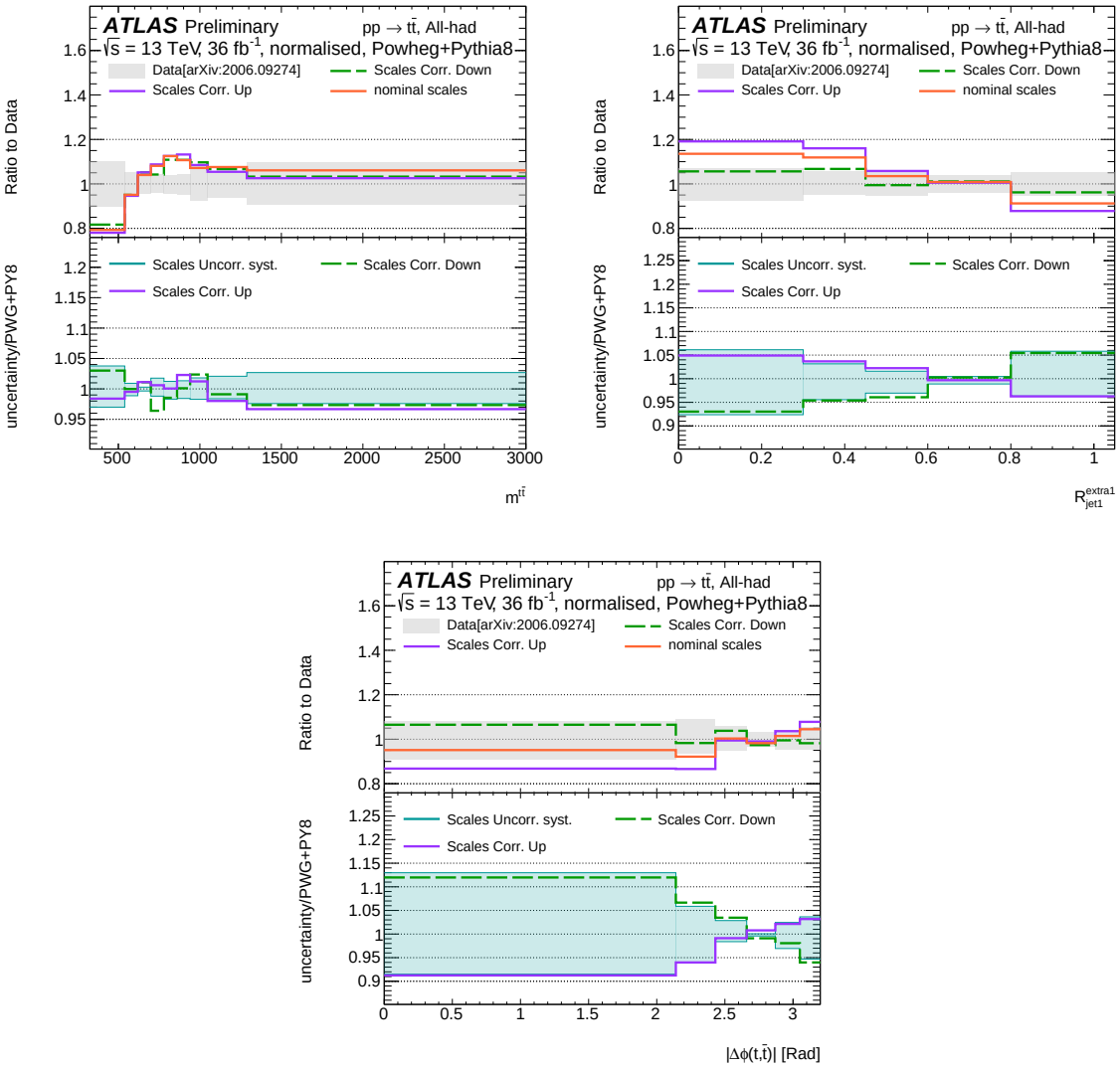

Figure 13: Differential $t\bar{t}$ production cross-section as a function of $m^{t\bar{t}}$ (top left), the ratio of the leading additional jet p_{T} to the leading jet p_{T} (top right), $\Delta\phi(t\bar{t})$ (bottom). All the distributions are normalised. In the top panel, the distributions show the correlated scale up and down choices, along with the nominal Powheg+Pythia 8 distribution, compared to the measured data. The uncertainty bands on these predictions are statistical only. The bottom panel shows the uncertainty on Powheg+Pythia 8 due to the scale variations uncorrelated in the hard-scatter and in the showering. The additional distributions in this panel show the coherent variation of the scale uncertainty in the hard-scatter and in the showering. The comparison is performed in the all-hadronic channel [53].

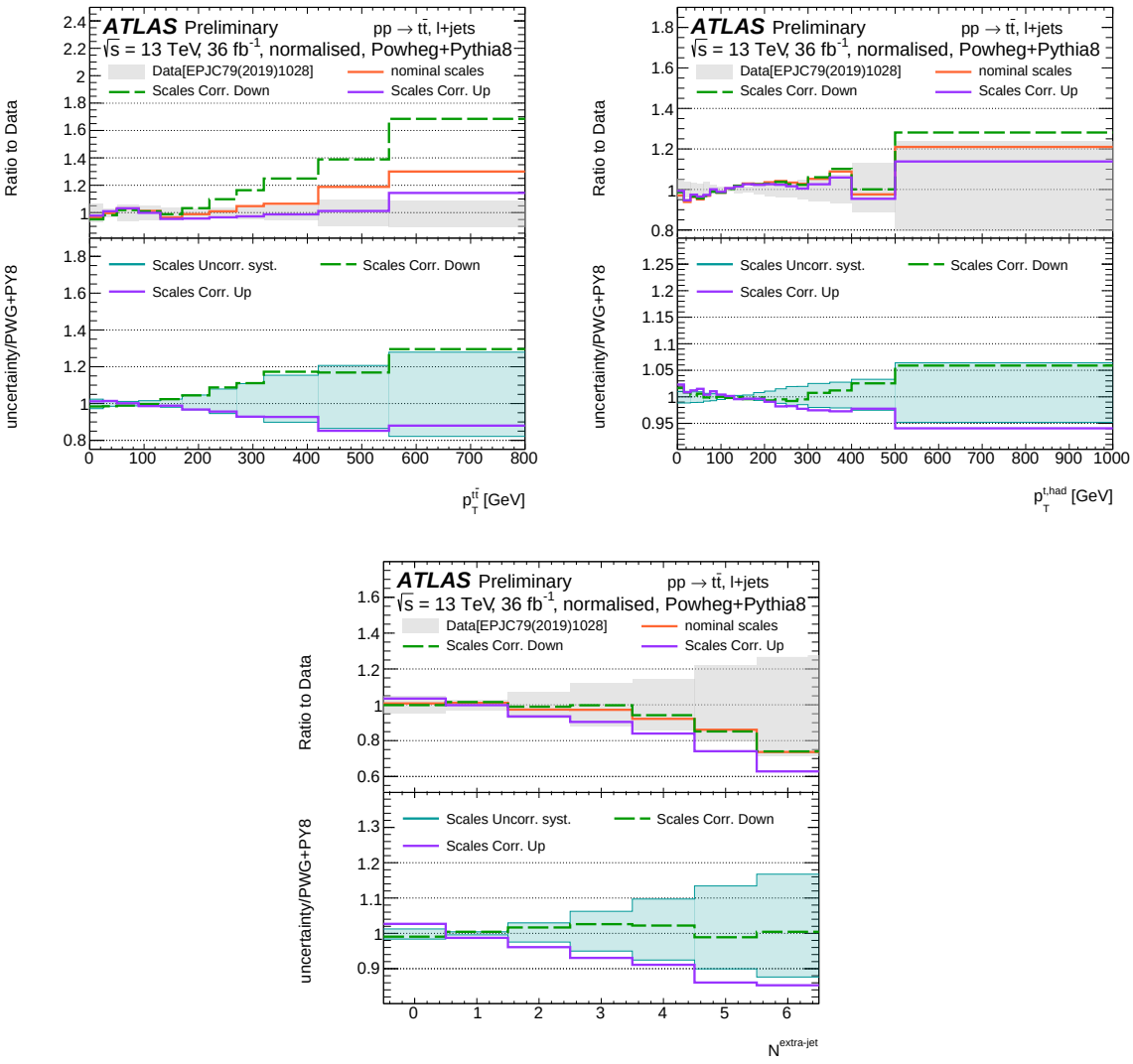

Figure 14: Differential $t\bar{t}$ production cross-section as a function of $p_{\mathrm{T}}^{t\bar{t}}$ (top left), $p_{\mathrm{T}}^{t,\mathrm{had}}$ (top right) and $N^{\text{extra-jet}}$ (bottom). All the distributions are normalised. In the top panel, the distributions show the correlated scale up and down choices, along with the nominal Powheg+Pythia 8 distribution, compared to the measured data. The uncertainty bands on these predictions are statistical only. The bottom panel shows the uncertainty on Powheg+Pythia 8 due to the scale variations uncorrelated in the hard-scatter and in the showering. The additional distributions in this panel show the coherent variation of the scale uncertainty in the hard-scatter and in the showering. The comparison is performed in the ℓ+jets channel [49].

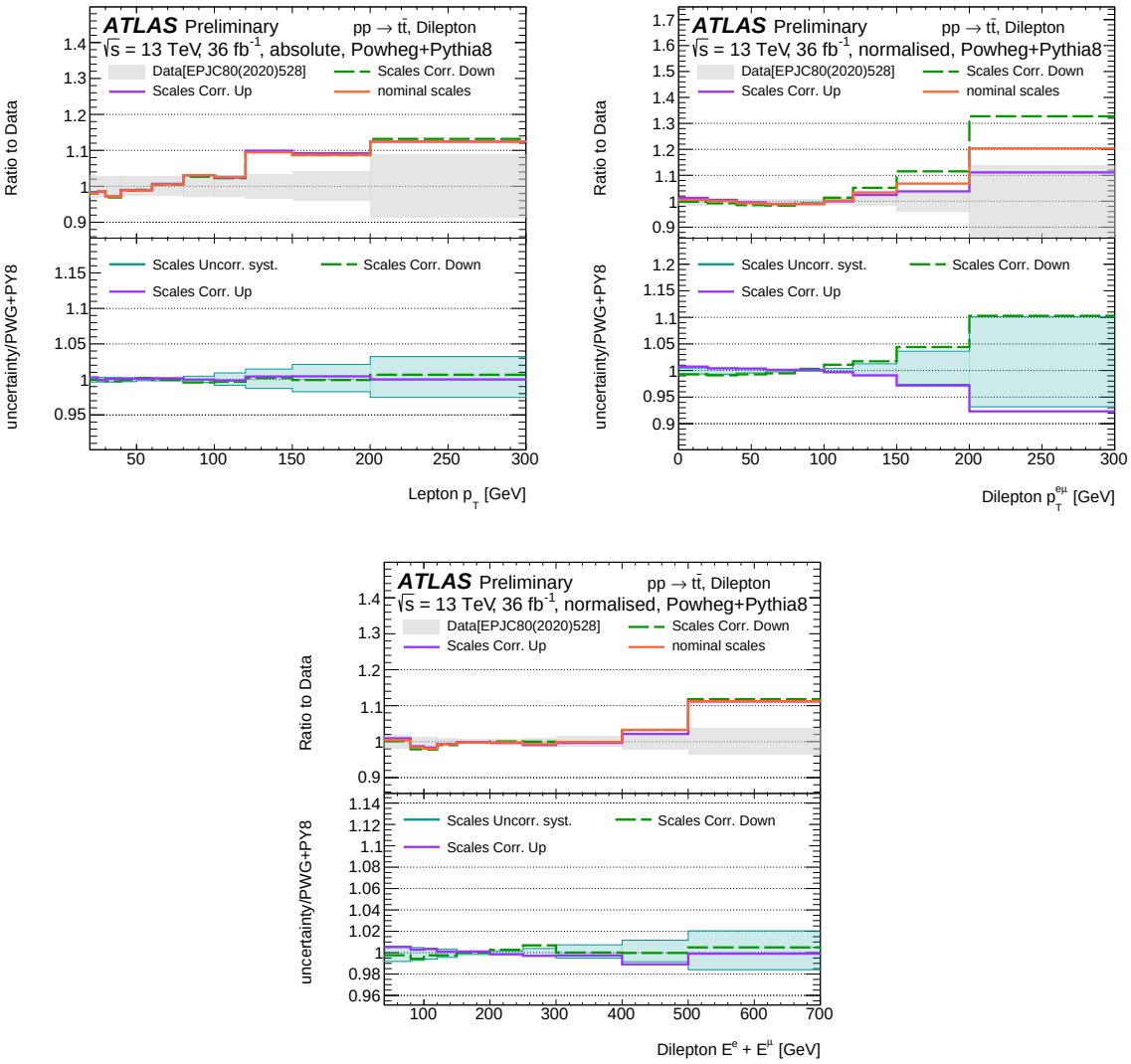

Figure 15: Differential $t\bar{t}$ production cross-section as a function of lepton p_{T} (top left), dilepton $p_{\mathrm{T}}^{e\mu}$ (top right) and dilepton $E^e + E^\mu$ (bottom). The top left distribution shows the absolute cross-section, while the normalised cross-section is shown in the other cases. In the top panel, the distributions show the correlated scale up and down choices, along with the nominal Powheg+Pythia 8 distribution, compared to the measured data. The uncertainty bands on these predictions are statistical only. The bottom panel shows the uncertainty on Powheg+Pythia 8 due to the scale variations uncorrelated in the hard-scatter and in the showering. The additional distributions in this panel show the coherent variation of the scale uncertainty in the hard-scatter and in the showering. The comparison is performed in the dilepton channel [52].

9 Shower recoils in the POWHEG+PYTHIA8 setup

In this section, the measured differential cross-sections are compared to several predictions obtained by changing the settings in POWHEG+PYTHIA8. The new configurations use alternative settings for the handling of the ISR or FSR recoil. By default the recoil of an ISR emission is taken by the whole final state while for the FSR the standard setting is to use a dipole, i.e. where only the emitting parton recoils against the emitted gluon. The sample labelled *ISR-dipoleRecoilOn* provides an alternative approach using local recoil for ISR, where only one outgoing parton takes the recoil of an ISR emission. In the sample labelled *ISR-rapidityOrderOff*, any emission after the first is ordered in rapidity, i.e. in terms of decreasing angles in a backwards-evolution sense. The standard ordering of emissions in POWHEG+PYTHIA8 is p_{T}-ordered. Finally, in the sample labelled *FSR-globalRecoilOn*, the first emission in FSR is recoiled against the whole event instead of the emitting parton.

The comparison between data and the new predictions is shown in Figures 16–22. In each figure, the upper pad shows the differential cross-section distribution for data and the predictions described above. In the second pad, the ratio to the data is shown for all predictions. The last two pads show the different components of the uncertainty which are summed in quadrature to form the purple band shown in the second pad. The components of the uncertainty are:

- *PS*: Uncertainty on parton shower and hadronisation, obtained as described in Section 7, using HERWIG7.1.3.
- h_{damp}: Uncertainty on the choice of the h_{damp} parameter that regulates the first emission, obtained as described in Section 8, using only h_{damp}=3.0 m_{top}.
- *ME(PY*)*: Uncertainty on the NLO+PS matching algorithm, obtained as described in Section 6.
- *PS ISR scales*: Uncertainty on ISR tuning, obtained as the envelope of the Up and Down variations of the A14 Var3c tune used in PYTHIA 8. This uncertainty corresponds to changing *SpaceShower:alphaSvalue* in the range [0.140, 0.115], with respect to the nominal value of 0.127. In terms of scale variations this corresponds to a scale variation of μ_R^{ISR}=[0.55, 1.96].
- *ME scales*: Uncertainty on the matrix element scales, using an envelope of the 7 points of the hard-scatter scale variations obtained by varying independently μ_R and μ_F by a factor 2.0 and 0.5.
- *PS FSR scales*: Uncertainty on FSR tuning, obtained by changing μ_R^{FSR} in the range [0.625, 2.0] with respect to the nominal scale.
- *ME PDF*: Uncertainty on the PDF in the matrix element, obtained by combining the 100 eigenvector variations of `NNPDF3.0NLO`.

For these plots, the ME(PY*) approach was used for the NLO+PS matching uncertainty but this should not be considered an endorsement of this method for all distributions.

There is no clear conclusion that can be drawn comparing the different channels. In general, the measurements from the single lepton analysis show a preference for the *dipoleRecoilOn* for variables related to the top p_{T}, such as $p_{\mathrm{T}}^{t,1}$ shown in Figure 19 (right) and $m^{t\bar{t}}$ in Figure 22 (left). This behaviour is consistent with the dilepton channel where the same prediction better describes the lepton p_{T}, shown in Figure 19 (left), and the dilepton p_{T}, shown in Figure 20 (left). The other distributions measured by the single-lepton and dilepton analyses are not particularly sensitive to the tested configurations. The all-hadronic channel seems to prefer the *rapidityOrderOff* sample, which gives the better prediction of

the fiducial cross-section as shown in Figure 16 (left), where the absolute cross-section is measured as a function of the $|y^{t\bar{t}}|$. In this channel the shape of several variables such as $\Delta\phi$ and all the p_{T} ratios are slightly better described by *rapidityOrderOff*. The leading top p_{T} distribution was measured in both the all-hadronic channel, shown in Figure 17, and in the single lepton channel, shown in Figure 19. Comparing these two figures it is clear that different topologies and phase-spaces prefer different configurations. A common observation between the two channels is that the *rapidityOrderOff* prediction overestimates the cross-section for high jet-multiplicity, with respect to what is observed in data, as shown in Figure 18 (right) and Figure 21 (right).

Even if some differences are observed in the agreement with the data when using these POWHEG+PYTHIA8 settings, the three predictions are all within the uncertainty band associated to the nominal prediction in almost every bin of every distribution, the only exception being events with high jet-multiplicity. The difference between the three predictions is even smaller than the PS uncertainty for several observables, as shown in all the distributions in the dilepton channel and from the leading top p_{T} in the ℓ+jets and all-hadronic analyses, shown in Figures 18–20.

It should be noted that the uncertainties of the nominal prediction differ significantly between observables. In all of the variables considered, the ME(PY*) and PS components are the dominant contribution with h_{damp} and ME scale variations gaining relevance in some extreme region of the phase-space such as in Figure 20 (left). The leading components of the uncertainty on the nominal prediction is strongly dependent on the observable. For example, the leading top and the $t\bar{t}$ system p_{T} in the all-hadronic analysis have very different uncertainties; in the former observable, the parton shower is the leading uncertainty while on the latter observable the ME scale variations and ME(PY*) are the dominant uncertainties.

On the p_{T} of the $t\bar{t}$ system, the h_{damp} uncertainty also plays a significant role, reaching 10% in the tail of the distribution in the all-hadronic channel, where ME(PY*) reaches 20%, and 18% in the ℓ+jets channel, where ME(PY*) reaches 27%. The most similar variable to $t\bar{t}$ in the dilepton channel is the dilepton p_{T} and here the h_{damp} uncertainty also gains relevance in the tail of the distribution, reaching $\approx$10%, while ME(PY*) reaches 15%. In the tails of the leading top p_{T} in the ℓ+jets channel, the ME(PY*) and h_{damp} uncertainties are at the same level and reach $\approx$10%, while at low p_{T} the two uncertainties are very different, with ME(PY*) being larger of $\approx$10%.

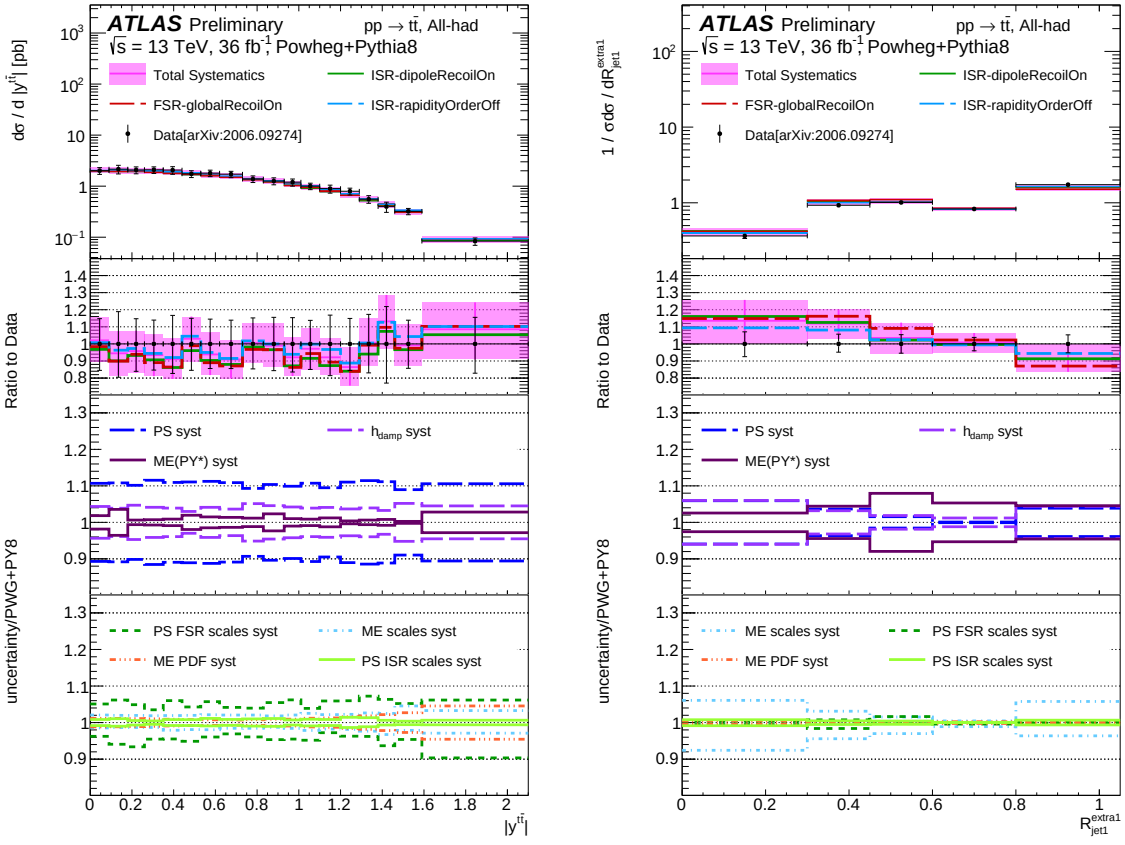

Figure 16: Differential $t\bar{t}$ production cross-section as a function of $|y^{t\bar{t}}|$ (left) and the ratio of the leading additional jet p_{T} to the leading jet p_{T} (right). In the upper pads, the data from [53] is compared to several predictions while the breakdown of the top-quark pair modelling uncertainties is presented in the bottom pads.

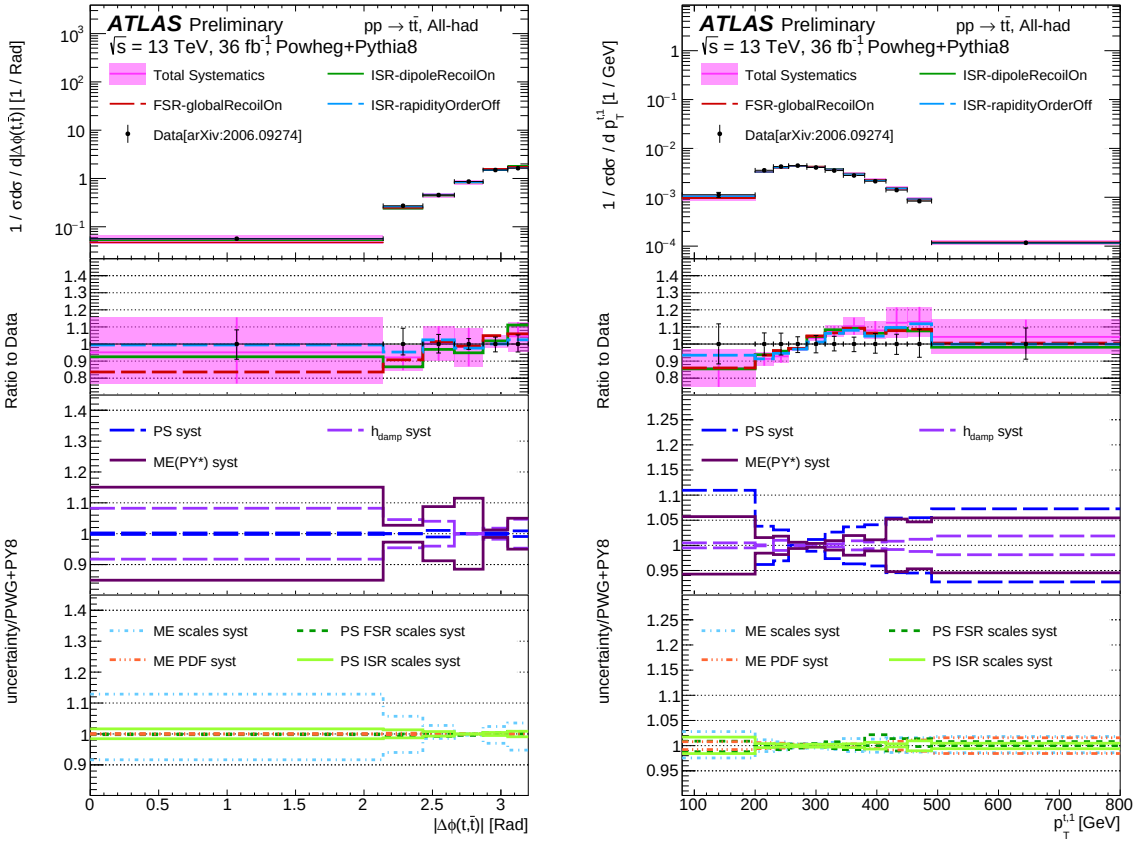

Figure 17: Differential $t\bar{t}$ production cross-section as a function of $|\Delta\phi(t,\bar{t})|$ (left) and $p_{\mathrm{T}}^{t,1}$ (right). In the upper pads, the data from [53] is compared to several predictions while the breakdown of the top-quark pair modelling uncertainties is presented in the bottom pads.

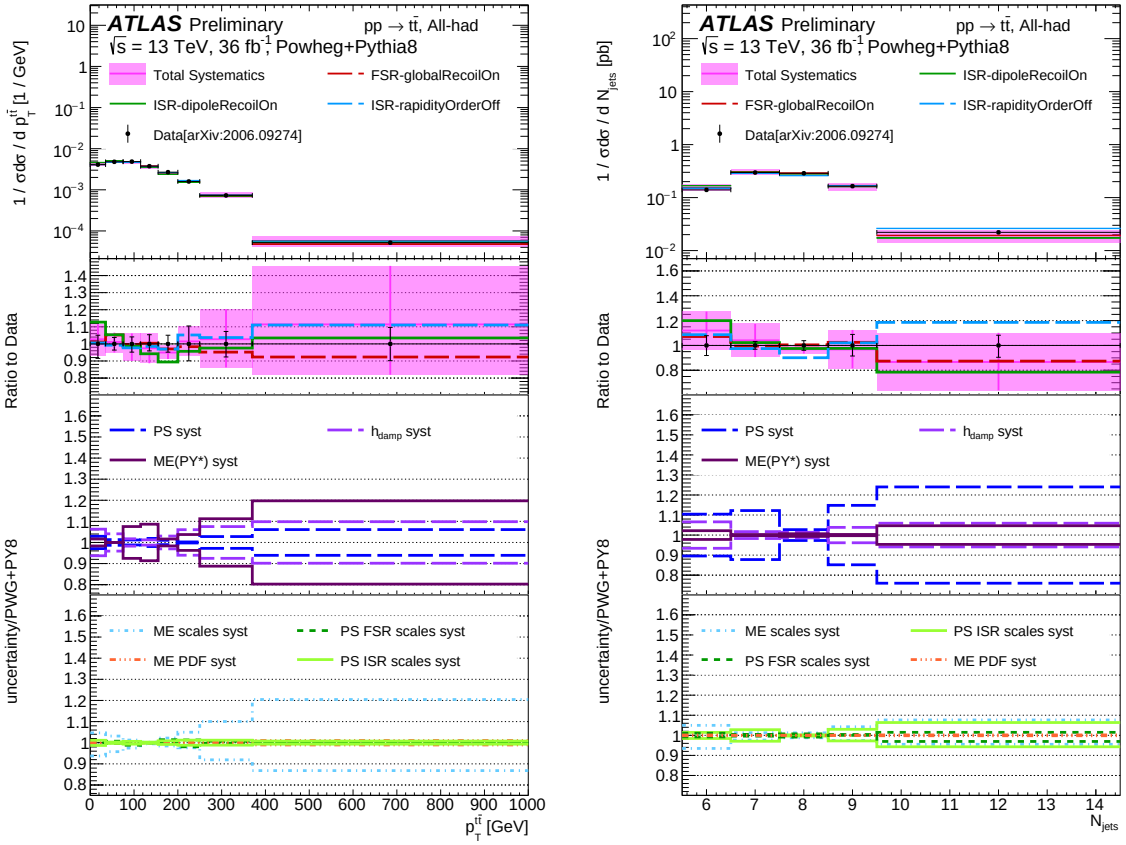

Figure 18: Differential $t\bar{t}$ production cross-section as a function of $p_{\mathrm{T}}^{t\bar{t}}$ (left) and number of jets (right). In the upper pads, the data from [53] is compared to several predictions while the breakdown of the top-quark pair modelling uncertainties is presented in the bottom pads.

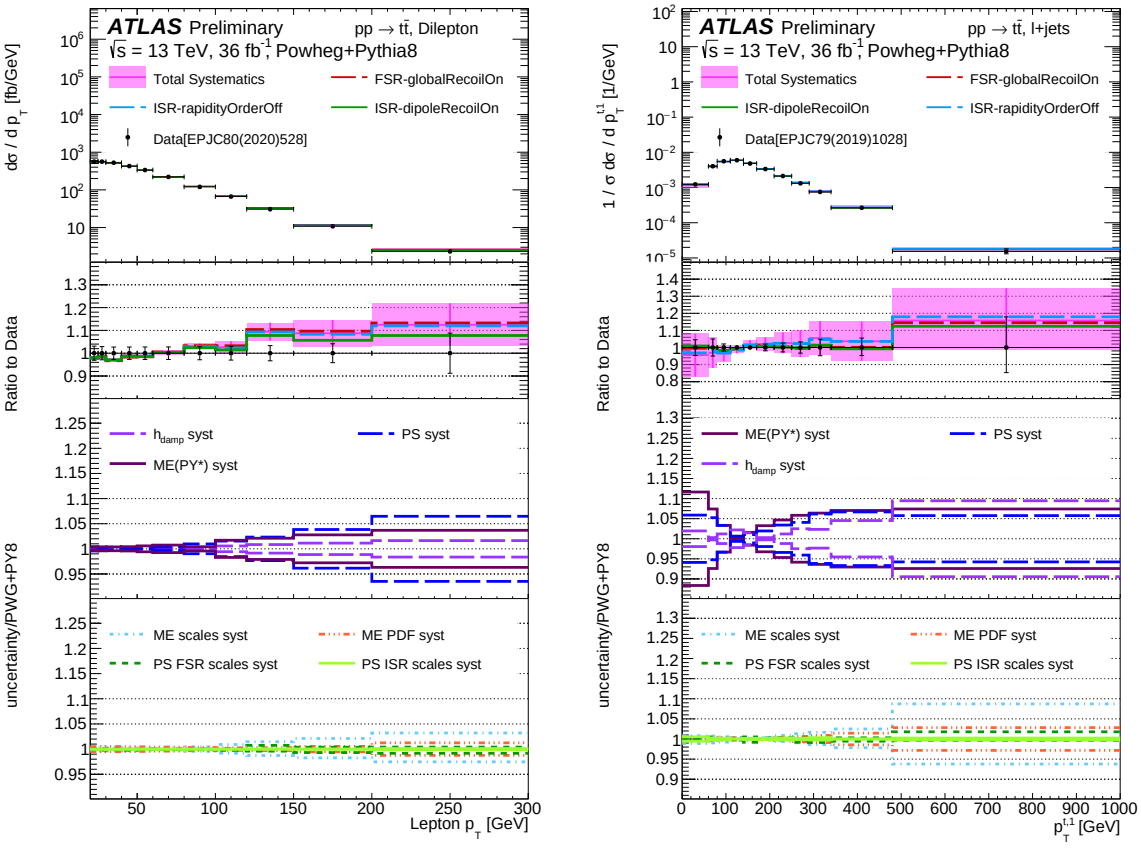

Figure 19: Differential $t\bar{t}$ production cross-section as a function of lepton p_{T} in the dilepton channel [52] (left) and $p_{\mathrm{T}}^{t,1}$ (right) in the ℓ+jets channel [49]. In the upper pads, the data is compared to several predictions while the breakdown of the top-quark pair modelling uncertainties is presented in the bottom pads.

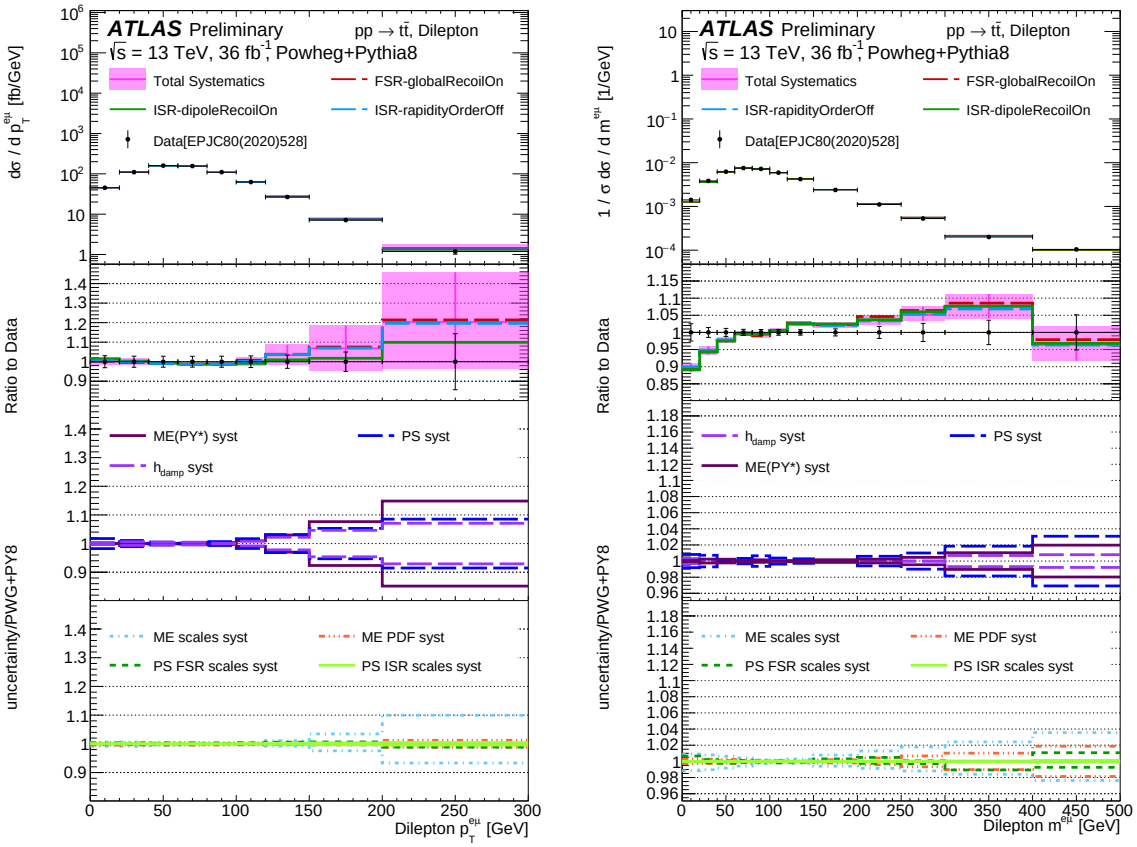

Figure 20: Differential $t\bar{t}$ production cross-section as a function of the dilepton system p_{T} (left) and the dilepton system mass (right). In the upper pads, the data from [52] is compared to several predictions while the breakdown of the top-quark pair modelling uncertainties is presented in the bottom pads.

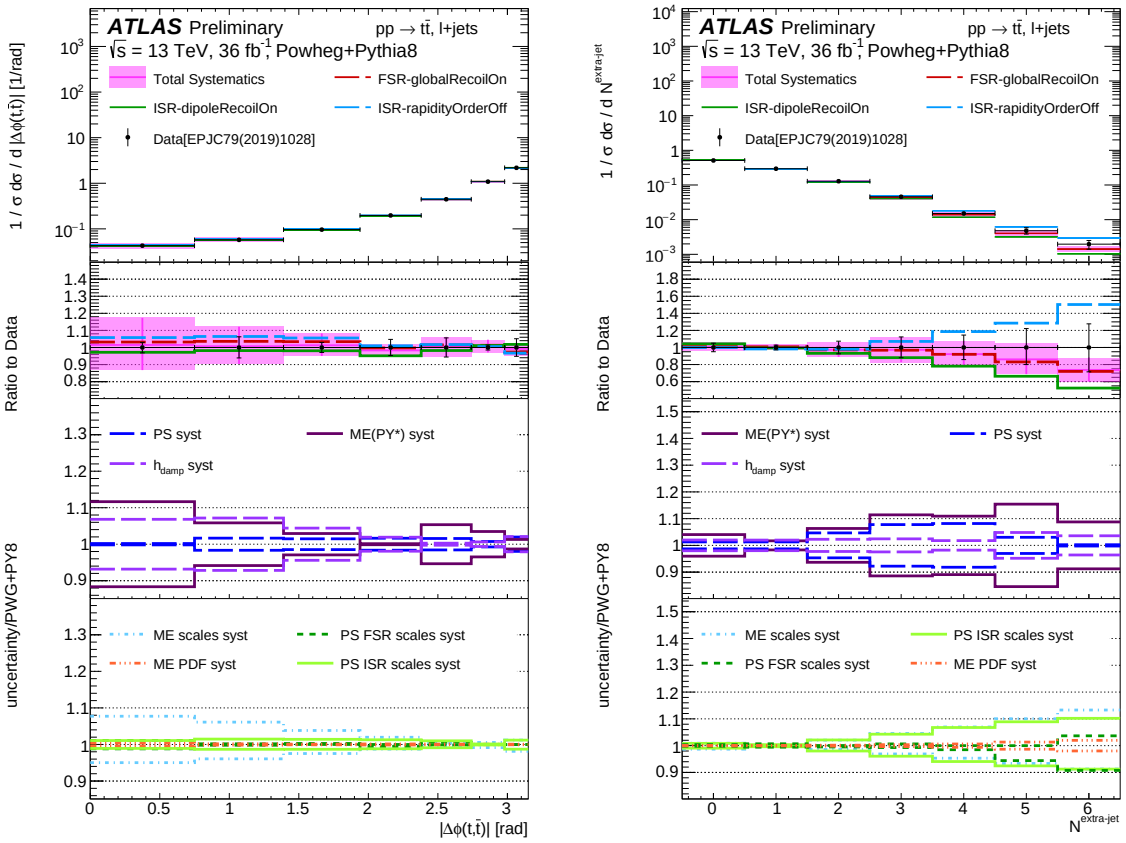

Figure 21: Differential $t\bar{t}$ production cross-section as a function of $|\Delta\phi(t,\bar{t})|$ between the two tops (left) and number of jets (right). In the upper pads, the data from [49] is compared to several predictions while the breakdown of the top-quark pair modelling uncertainties is presented in the bottom pads.

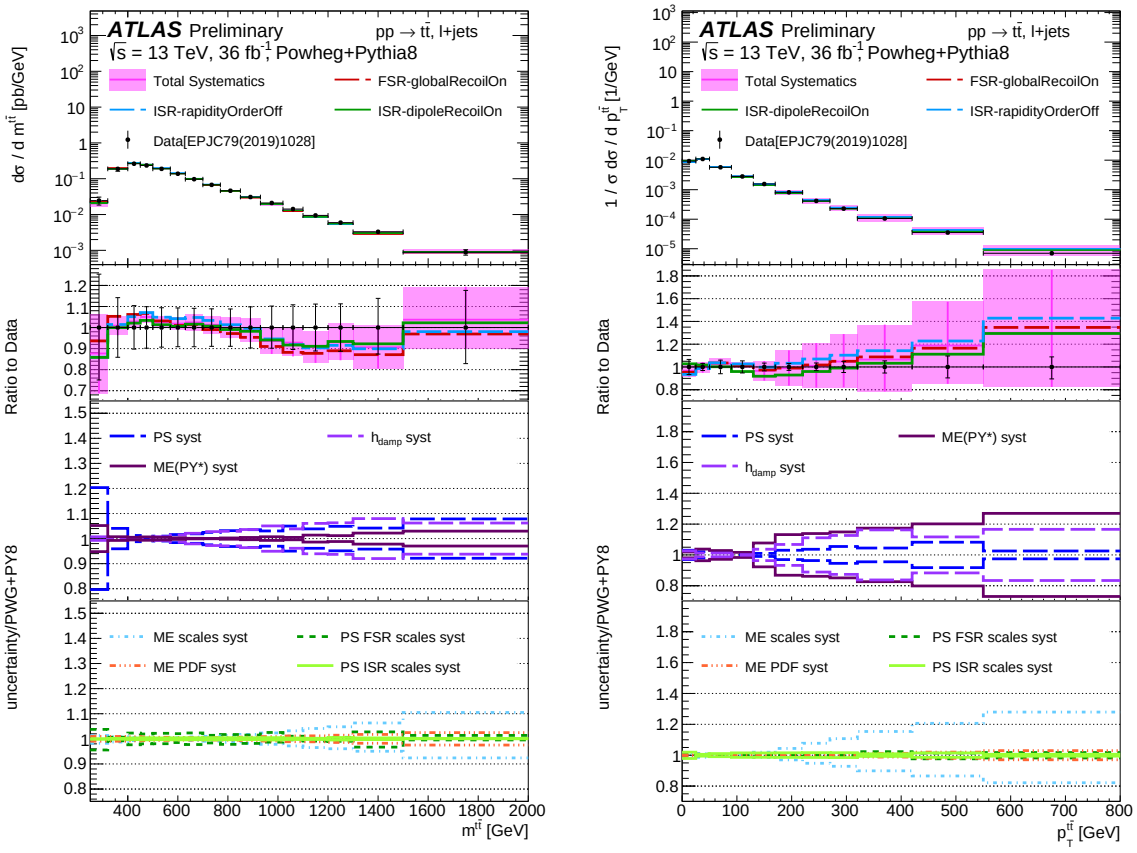

Figure 22: Differential $t\bar{t}$ production cross-section as a function of $m^{t\bar{t}}$ (left) and $p_{\mathrm{T}}^{t\bar{t}}$ (right). In the upper pads, the data from [49] is compared to several predictions while the breakdown of the top-quark pair modelling uncertainties is presented in the bottom pads.

10 NLO-merged predictions

In this section, SHERPA 2.2.8 is used to produce multi-leg predictions for top-quark pair production and the corresponding uncertainty is estimated using an approach where all the variations are done within SHERPA. The details of the MC sample is described in Section 2. Moreover a set of perturbative uncertainties on the SHERPA 2.2.8 prediction is also defined and presented here.

10.1 Definition of the uncertainty components

A perturbative uncertainty on the SHERPA 2.2.8 prediction is obtained by summing in quadrature several components estimated by varying the following parameters:

- $\mu^{ME} = \mu^{PS} = [0.5, 2.0]$: An estimate of the missing higher-order uncertainties is obtained from 7-point variations of the renormalisation (μ_R) and factorisation (μ_F) perturbative scales, obtained by varying up and down by a factor of two independently and coherently. These variations are propagated in a correlated way to the parton shower.
- $PDF + \alpha_S$: Uncertainty on the PDF set and α_S used in the hard-scatter and the parton showering. It is obtained as the sum in quadrature of two components. The first is the standard deviation from the `NNPDF3.0nnlo` [12] replicas and the second is obtained from the α_S variations of ± 0.001 around the nominal value of 0.118.
- Q_{cut}: Defines the scale used for the multi-jet merging. The scale is set to 30 GeV, with variations of 50 GeV and 20 GeV.
- μ_{Q}: Regulates the parton shower starting scale. The nominal resummation scale is varied by factors of 2.0 and 0.5.
- *PS recoil*: Changes the recoil strategy for dipoles in the parton shower. The default uses `CSS_KIN_SCHEME` set to 1 and corresponds to the scheme described in [23], while the variation is obtained by setting `CSS_KIN_SCHEME` to 0. This last setting corresponds to the recoil scheme described in [58].

The $\mu^{ME} = \mu^{PS} = [0.5, 2.0]$ and $PDF + \alpha_S$ are obtained using internal reweighting [59] of the sample. Several kinematic observables of the top-quark and the $t\bar{t}$ system are presented in Figures 23–25. In the top pad of each figure, the nominal SHERPA 2.2.8 prediction is shown together with the total perturbative uncertainty and is compared to the differential $t\bar{t}$ cross-section measured by the ATLAS experiment in the ℓ+jets channel. The SHERPA 2.2.8 prediction includes approximate NLO EW corrections calculated using the NLO EW_{virt} approach [34]. In the middle and bottom pads, the breakdown of the components of the total perturbative uncertainty band are reported.

In general, SHERPA 2.2.8 shows a good agreement with the measured cross-sections, in particular with $|\Delta\phi(t,\bar{t})|$, $N^{\text{extra-jets}}$ and $p_{\text{T}}^{t,\text{had}}$ where the baseline predictions are largely inside the uncertainty band for the measurement. For $m^{t\bar{t}}$ and $p_{\text{T}}^{t\bar{t}}$ the agreement is at the edge of the uncertainty on the prediction in some region of the spectra. The distribution showing the worst agreement is $\chi^{t\bar{t}}$, where the prediction underestimates the data for a large part of the spectrum and both the uncertainty on the measurement and the prediction are below 5%. The electroweak corrections have a very small impact on the distributions considered, showing an impact only in the tails of the $p_{\text{T}}^{\text{top}}$ where they slightly improve the agreement between the prediction and the data. The dominant uncertainty component depends on the distribution, but

the perturbative scale uncertainties and the Q_{cut} merging scale are dominant in most bins for the majority of the observables. The scale uncertainties dominate on the full $|\Delta\phi(t,\bar{t})|$ spectrum and in the low $p_{\text{T}}^{t\bar{t}}$ and $N^{\text{extra-jets}}$ regions, while at high $p_{\text{T}}^{t\bar{t}}$ and $N^{\text{extra-jets}}$ the Q_{cut} merging becomes comparable to the scale uncertainty. On $m^{t\bar{t}}$ the CSS recoil uncertainty is significant, at the same level of the perturbative scale variations. The uncertainties on the $\chi^{t\bar{t}}$ are quite flat and around 5% along the full spectrum, while for the other observables they start from 4–5% and then increase, reaching up to 30–40% in the tails of the $p_{\text{T}}^{t\bar{t}}$ and $N^{\text{extra-jets}}$ distributions.

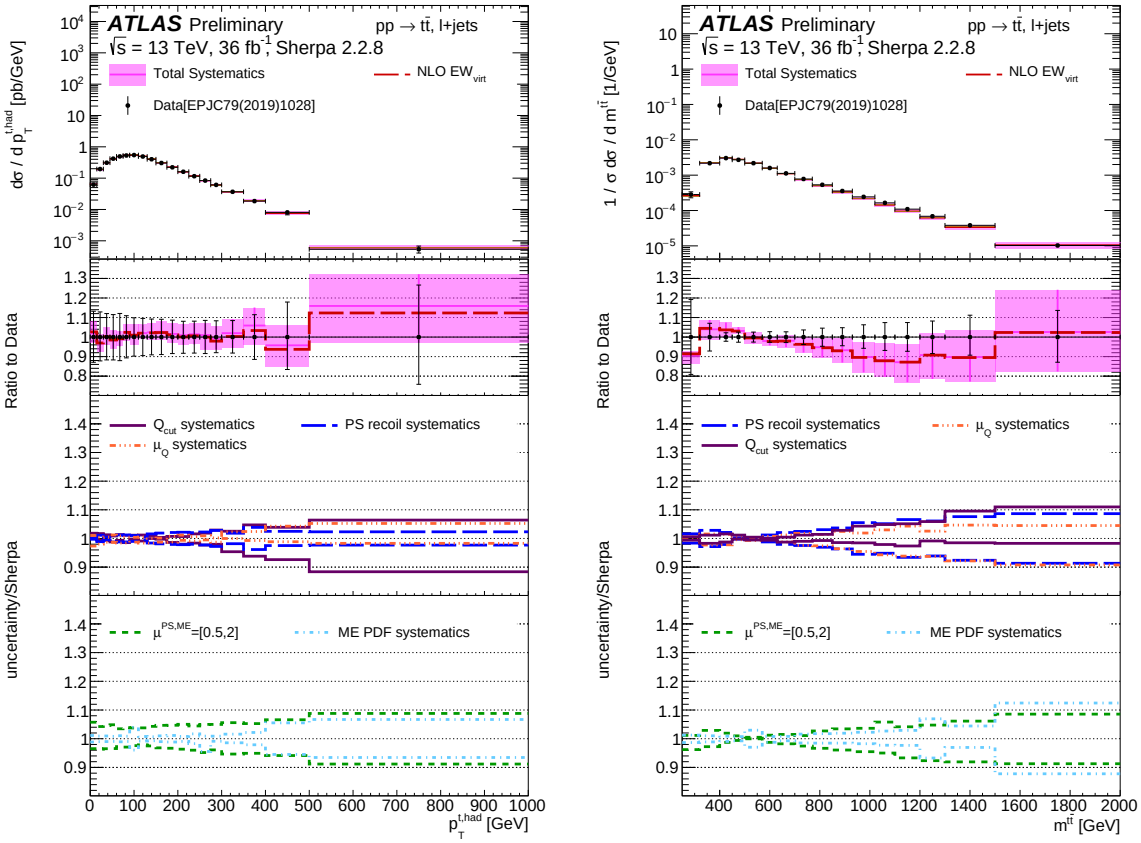

Figure 23: Distribution of the $t\bar{t}$ production cross-section as a function of the $p_{\mathrm{T}}^{t,\mathrm{had}}$ (left) and $m^{t\bar{t}}$ (right) for data and the Sherpa 2.2.8 (nominal) Monte Carlo samples using the nominal parameters and with the addition of the electroweak (EW) corrections. The left plot shows an absolute cross-section while the right one shows a normalised distribution. The total systematic uncertainty band represents the sum in quadrature of the uncertainties related to the scale in the matrix element and showering, PDF variations, the choice of the Q_{cut} matching scale, the resummation scale (μ_{Q}) and the CSS dipole recoil scheme. The alternative prediction with the electroweak corrections includes statistical uncertainties only. The first panel shows the ratio of each sample to the nominal Sherpa 2.2.8 prediction. The other panels show separately each uncertainty component. The comparison is performed in a ℓ+jets channel which requires a single electron or muon and four or more jets, at least two of which are b-jets. The fiducial selection is detailed in [49].

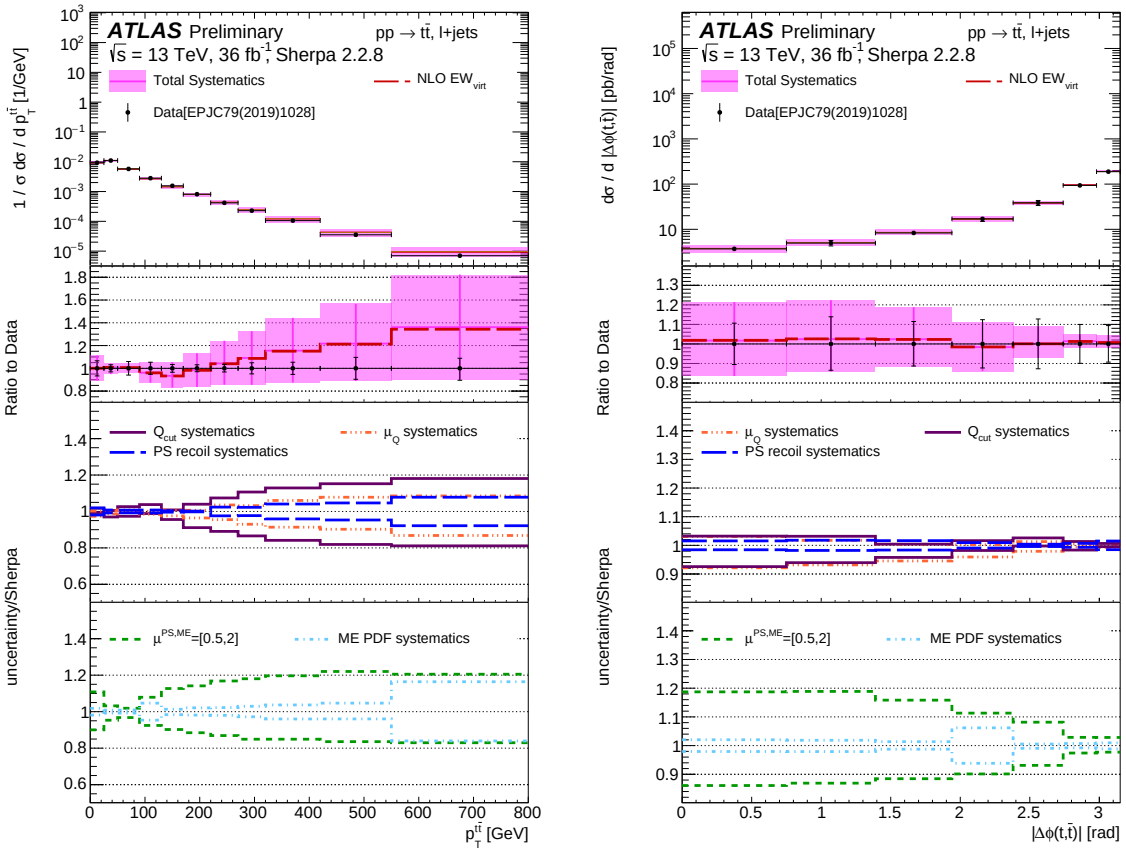

Figure 24: Distribution of the $t\bar{t}$ production cross-section as a function of the $p_{\mathrm{T}}^{t\bar{t}}$ (left) and $|\Delta\phi(t,\bar{t})|$ (right) for data and the Sherpa 2.2.8 (nominal) Monte Carlo samples using the nominal parameters and with the addition of the electroweak (EW) corrections. The left plot shows an absolute cross-section while the right one shows a normalised distribution. The total systematic uncertainty band represents the sum in quadrature of the uncertainties related to the scale in the matrix element and showering, PDF variations, the choice of the Q_{cut} matching scale, the resummation scale (μ_{Q}) and the CSS dipole recoil scheme. The alternative prediction with the electroweak corrections includes statistical uncertainties only. The first panel shows the ratio of each sample to the nominal Sherpa 2.2.8 prediction. The other panels show separately each uncertainty component. The comparison is performed in a ℓ+jets channel which requires a single electron or muon and four or more jets, at least two of which are b-jets. The fiducial selection is detailed in [49].

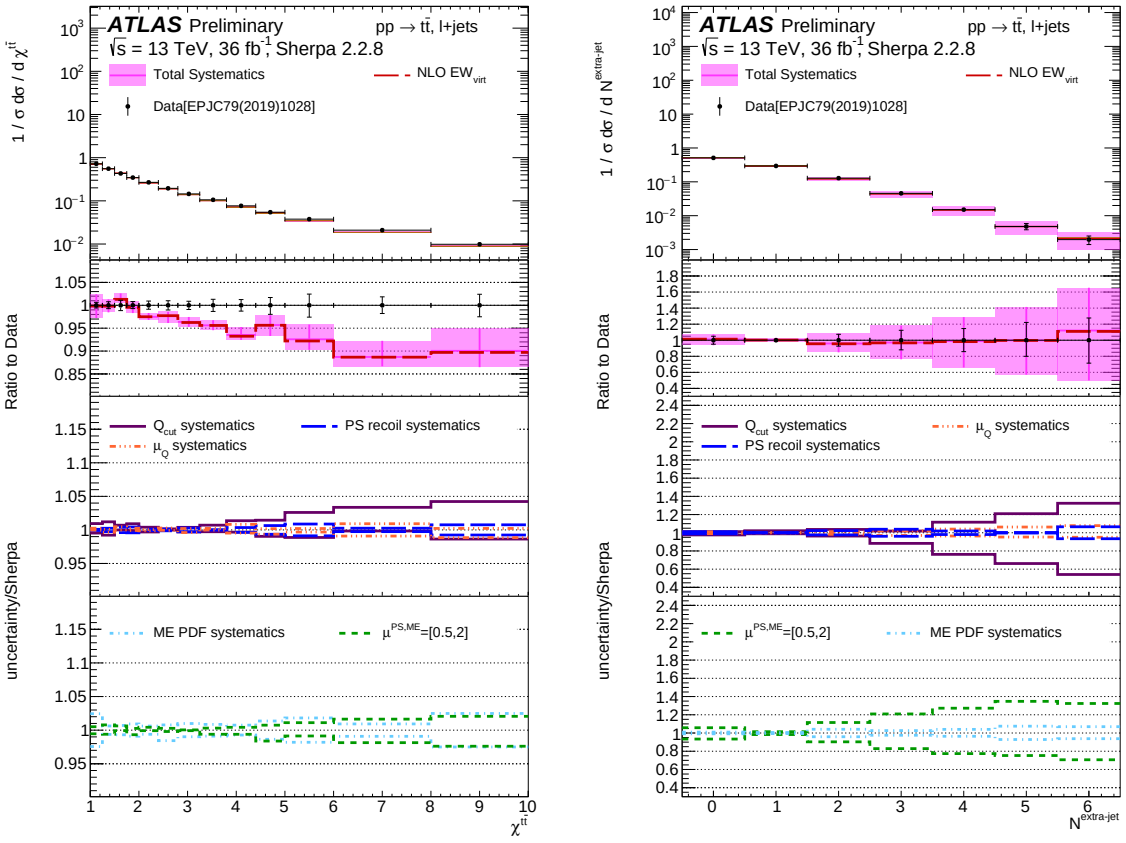

Figure 25: Distribution of the $t\bar{t}$ production cross-section as a function of the $\chi^{t\bar{t}}$ (left) and N_{jets}^{extra} (right) for data and the SHERPA 2.2.8 (nominal) Monte Carlo samples using the nominal parameters and with the addition of the electroweak (EW) corrections. The left plot shows an absolute cross-section while the right one shows a normalised distribution. The total systematic uncertainty band represents the sum in quadrature of the uncertainties related to the scale in the matrix element and showering, PDF variations, the choice of the Q_{cut} matching scale, the resummation scale (μ_{Q}) and the CSS dipole recoil scheme. The alternative prediction with the electroweak corrections includes statistical uncertainties only. The first panel shows the ratio of each sample to the nominal SHERPA 2.2.8 prediction. The other panels show separately each uncertainty component. The comparison is performed in a ℓ+jets channel which requires a single electron or muon and four or more jets, at least two of which are b-jets. The fiducial selection is detailed in [49].

10.2 Comparison to the Powheg+Pythia 8 setup

Since the beginning of LHC Run 2, Powheg+Pythia 8 has been the nominal generator used to describe the $t\bar{t}$ process in ATLAS, and its showering parameters have been tuned to data [3, 13] to improve the agreement with the measurements. The Sherpa 2.2.8 generator employs a more sophisticated treatment of the additional emissions and matching to the parton shower, that should improve the agreement with the data and the precision, but has never been extensively compared to measured differential cross-sections or tuned to data. The aim of this comparison is to verify if the Sherpa 2.2.8 predictions are able to describe the data on several observables, at least at the same level of the current nominal prediction employed in ATLAS. This comparison is also the first look at the uncertainty band associated to Sherpa 2.2.8 in $t\bar{t}$ predictions and to how this compares to the set of uncertainty associated to Powheg+Pythia 8, that are the results of a long set of studies and refinements [1]. The long term aim of this study is to facilitate the usage in ATLAS of NLO-merged generators for the $t\bar{t}$ prediction. The uncertainty associated to Powheg+Pythia 8 are the same described in Section 9, with a few modifications to define a set of uncertainties coherent with the effects considered in the Sherpa 2.2.8 uncertainty band, described in Section 10.1.

- The uncertainty on the matching ME(PY8*) has been removed from the band
- The uncertainty on parton shower and hadronisation is evaluated as the symmetrised difference between the nominal Powheg+Pythia 8 and the sample with the *ISR-dipoleRecoilOn*. This uncertainty should be equivalent to the *CSS recoil* component considered for Sherpa 2.2.8.

After these changes to the Powheg+Pythia 8 perturbative uncertainty breakdown, the two generators have a set of uncertainties aiming to address the same ambiguities in both predictions. The only exception is the Q_{cut} component in Sherpa 2.2.8 which covers the merging scale variation which is only defined for multi-leg generators and does not have a counterpart in Powheg+Pythia 8. In the upper panels of Figures 26 and 27, the nominal predictions obtained from the two generators are compared with the measured $t\bar{t}$ production cross-section as a function of $p_{\text{T}}^{t,\text{had}}$,$m^{t\bar{t}}$,$p_{\text{T}}^{t\bar{t}}$, $|\Delta\phi(t,\bar{t})|$, $\chi^{t\bar{t}}$ and $N^{\text{extra-jets}}$. The nominal predictions here are reported only with the statistical uncertainty. In the bottom panels the uncertainties obtained with the two strategies are directly compared. Both Powheg+Pythia 8 and Sherpa 2.2.8 show a good agreement with the data on several observables, with the largest disagreement with the measurement observed in the tail of the $p_{\text{T}}^{t\bar{t}}$, shown in Figure 26 (right). However, the difference is still smaller than the uncertainty on the predictions, that in this region reaches 30% for both the generators.

The $\chi^{t\bar{t}}$ distribution, shown in Figure 27, presents differences between the two predictions. Here the uncertainty obtained with Sherpa is significantly lower and the agreement with the data is worse than the one obtained from the Powheg+Pythia 8 prediction. The largest difference among the two predictions is observed at high $N^{\text{extra-jets}}$ multiplicity (> 3 jets), where Sherpa 2.2.8 overestimates the data and Powheg+Pythia 8 underestimates them, while remaining inside the measured uncertainty band. The modelling of both predictions in this region are dominated by the showering. The lower jet multiplicities drove the choice of h_{damp} when tuning Powheg+Pythia 8 to $t\bar{t}$ data [1, 3], so the good agreement observed is expected. Across all the spectra investigated, Sherpa 2.2.8 shows a larger uncertainty with respect to Powheg+Pythia 8 on the majority of the spectrum. The difference between the two uncertainties is of only few percent on $m^{t\bar{t}}$ and $p_{\text{T}}^{t,\text{had}}$ but reaches 10% on $|\Delta\phi(t,\bar{t})|$ and $N^{\text{extra-jets}}$. A smaller uncertainty band on Powheg+Pythia 8 was not expected, as the approach used in the Sherpa 2.2.8 prediction is more sophisticated. This seems to be caused mainly by the perturbative scale uncertainty, which in Sherpa 2.2.8 is significantly larger than the corresponding uncertainty for Powheg+Pythia 8. One source of difference in the uncertainty is the approach used to estimate the scale variation in the showering; in Sherpa 2.2.8 the

μ_R and μ_F scales are varied by a factor 2.0 coherently with the matrix element, whereas the variation of scales in the showering for Powheg+Pythia 8 are motivated from a tuning to ATLAS data [13]. Here the variation corresponds to μ_R^{ISR}[0.55,1.96] and μ_R^{FSR}[0.625,2.0], and are modified independently from the hard-scatter scale variations. Another important difference in the scale uncertainty is the treatment of the Sudakov reweighting of the first emission which is not considered in the Powheg+Pythia 8 setup and could justify the larger uncertainty on Sherpa 2.2.8. In addition, the PDF uncertainty in Sherpa 2.2.8 is propagated through the full calculation, including the parton shower, whereas in Powheg+Pythia 8 the effect is limited to the hard-scatter simulation.

In summary, both the Powheg+Pythia 8 and Sherpa 2.2.8 predictions give a similar description of the data, with the impact of the EW corrections being small. The Sherpa uncertainties are slightly larger than those currently used in $t\bar{t}$ measurements, and is worth further investigation in the future.

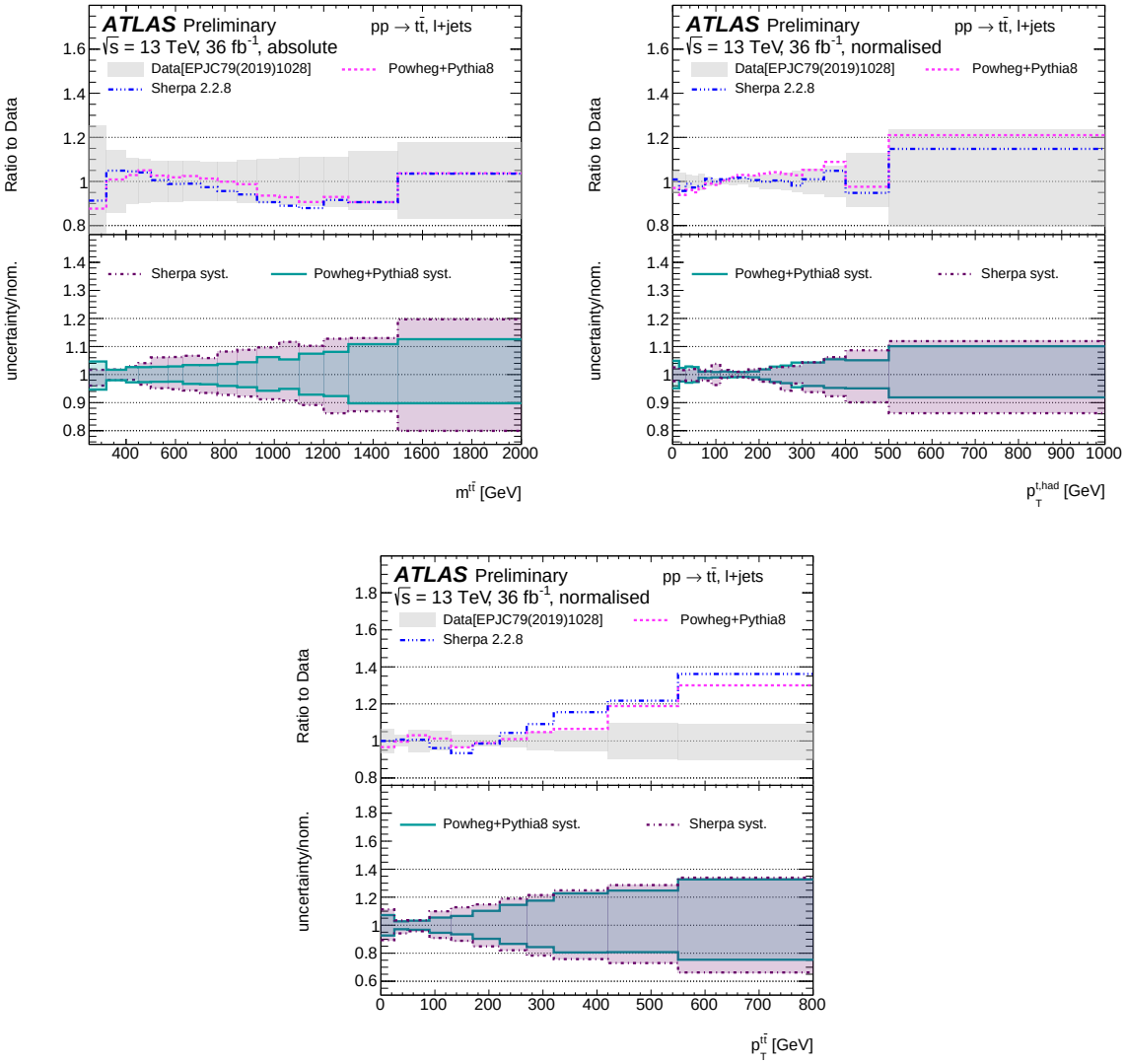

Figure 26: In the top panel, the measured distribution of the $t\bar{t}$ production cross-section as a function of the $p_{\mathrm{T}}^{t,\mathrm{had}}$ (top left), $m^{t\bar{t}}$ (top right) and $p_{\mathrm{T}}^{t\bar{t}}$ (bottom) is compared with Sherpa 2.2.8 and Powheg+Pythia 8, where only the statistical component is included as uncertainty on the MC prediction, while the data are reported with the full uncertainty band. The top left plot shows an absolute cross-section while the top right and the bottom show the comparison among normalised distributions. In the bottom panel the total uncertainty bands derived on the two models on the absolute cross-section are compared. The comparison is performed in a ℓ+jets channel [49].

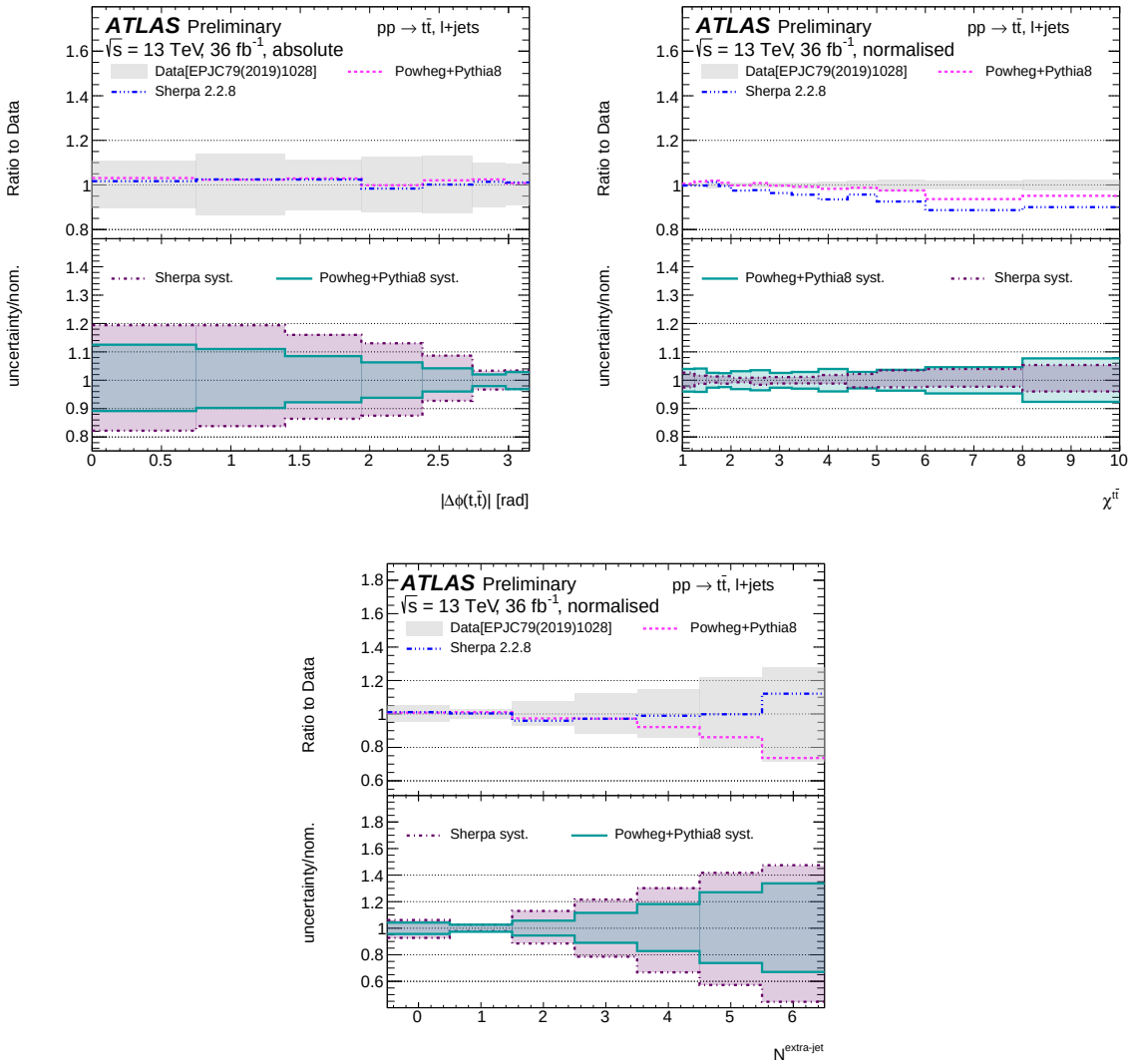

Figure 27: In the top panel, the measured distribution of the absolute $t\bar{t}$ production cross-section as a function of the $|\Delta\phi(t,\bar{t})|$ (top left), $\chi^{t\bar{t}}$ (top right) and $N^{\text{extra-jets}}$ (bottom) is compared with SHERPA 2.2.8 and POWHEG+PYTHIA 8, where only the statistical component is included as uncertainty on the MC prediction, while the data are reported with the full uncertainty band. The top left plot shows an absolute cross-section while the top right and bottom show the comparison among normalised distributions. In the bottom panel the total uncertainty bands derived on the two models on the absolute cross-section are compared. The comparison is performed in a ℓ+jets channel [49].

11 Conclusion

Various MC generators and settings were studied and used to investigate the modelling uncertainties for top-quark pair production. Their predictions were compared to recent ATLAS measurements in three different top-quark decay channels using an integrated luminosity of 36.1 fb^{-1} of $\sqrt{s}$ = 13 TeV data.

Alternative approaches for estimating the NLO+PS matching uncertainty were examined using alternative samples. This highlighted how the previous approach convolved two effects: a difference in the matching algorithm and a difference in the matrix-element corrections applied by the parton shower. This resulted in a larger uncertainty when compared to the two new approaches introduced in this note, where more consistent showering settings were used. Differences between the two new approaches were also observed, suggesting that also the new estimates of the NLO+PS matching uncertainty include remaining effects beyond the pure algorithmic differences.

The parton shower uncertainty is evaluated with a comparison of the nominal sample and Powheg +Herwig7 with two versions: 7.0.4 and 7.1.3. The differences among the two samples are rather small, but the sample showered with Herwig7.1.3 provides slightly better agreement with the data. A switch to version 7.1.3 would result in a small increase in the uncertainties on some observables, due to the larger differences with the nominal prediction compared with version 7.0.4.

Studies on the h_{damp} and scale variations in Powheg +Pythia 8 are also presented. The usage of a down variation of the h_{damp} parameter, h_{damp}= 0.75 m_{top}, yields results similar to the symmetrisation of the uncertainty obtained comparing Powheg +Pythia 8 with h_{damp}= 1.5 m_{top} and h_{damp}= 3.0 m_{top}, suggesting that the symmetrised uncertainty band can be used instead of generating an alternative sample. Studies of the scale variations in the hard-scatter and the showering showed that the uncertainty resulting from the different correlations studied are very similar.

In addition to studies on the top modelling uncertainties, several new Powheg +Pythia 8 samples with different showering parameters were studied and compared to data. All the showering variations considered fall within the uncertainty band associated to Powheg +Pythia 8, except in very extreme regions of the phase-space. All the samples describe quite well the data from the three analyses, but the level of agreement is strongly dependent on the phase-space and the observable with no clear configuration being preferred to improve the overall description of the data. More quantitative studies are needed in order to define a new standard general-purpose baseline sample.

Finally, a Sherpa 2.2.8 sample was produced to define a new set of modelling uncertainties within a single generator and its prediction was compared to both the data and to the nominal Powheg +Pythia 8 setup. In general, the predictions obtained with Sherpa 2.2.8 show a good agreement with the ATLAS data for several observables, qualitatively at the same level of Powheg +Pythia 8. The uncertainty evaluated for the Sherpa 2.2.8 prediction appears similar to the current approach, with some exception in the more extreme regions of phase-space.

References

[1] ATLAS Collaboration, *Improvements in $t\bar{t}$ modelling using NLO+PS Monte Carlo generators for Run 2*, ATL-PHYS-PUB-2018-009, 2018, URL: https://cds.cern.ch/record/2630327 (cit. on pp. 3, 6, 44).

[2] ATLAS Collaboration, *Studies on top-quark Monte Carlo modelling with Sherpa and MG5_aMC@NLO*, ATL-PHYS-PUB-2017-007, 2017, URL: https://cds.cern.ch/record/2261938 (cit. on pp. 3, 4, 6).

[3] ATLAS Collaboration, *Studies on top-quark Monte Carlo modelling for Top2016*, ATL-PHYS-PUB-2016-020, 2016, URL: https://cds.cern.ch/record/2216168 (cit. on pp. 3, 4, 6, 21, 44).

[4] ATLAS Collaboration, *Further studies on simulation of top-quark production for the ATLAS experiment at $\sqrt{s}$ = 13 TeV*, ATL-PHYS-PUB-2016-016, 2016, URL: https://cds.cern.ch/record/2205262 (cit. on pp. 3, 6).

[5] ATLAS Collaboration, *Simulation of top-quark production for the ATLAS experiment at $\sqrt{s}$ = 13 TeV*, ATL-PHYS-PUB-2016-004, 2016, URL: https://cds.cern.ch/record/2120417 (cit. on pp. 3, 6).

[6] S. Frixione, P. Nason and G. Ridolfi, *A positive-weight next-to-leading-order Monte Carlo for heavy flavour hadroproduction*, JHEP **09** (2007) 126, arXiv: 0707.3088 [hep-ph] (cit. on pp. 3, 4, 9).

[7] P. Nason, *A new method for combining NLO QCD with shower Monte Carlo algorithms*, JHEP **11** (2004) 040, arXiv: hep-ph/0409146 (cit. on pp. 3, 4, 9).

[8] S. Frixione, P. Nason and C. Oleari, *Matching NLO QCD computations with parton shower simulations: the POWHEG method*, JHEP **11** (2007) 070, arXiv: 0709.2092 [hep-ph] (cit. on pp. 3, 4, 9).

[9] S. Alioli, P. Nason, C. Oleari and E. Re, *A general framework for implementing NLO calculations in shower Monte Carlo programs: the POWHEG BOX*, JHEP **06** (2010) 043, arXiv: 1002.2581 [hep-ph] (cit. on pp. 3, 4, 9).

[10] T. Sjöstrand et al., *An introduction to PYTHIA 8.2*, Comput. Phys. Commun. **191** (2015) 159, arXiv: 1410.3012 [hep-ph] (cit. on pp. 3, 4).

[11] E. Bothmann et al., *Event Generation with Sherpa 2.2*, SciPost Phys. **7** (2019) 034, arXiv: 1905.09127 [hep-ph] (cit. on pp. 3, 4).

[12] R. D. Ball et al., *Parton distributions for the LHC Run II*, JHEP **04** (2015) 040, arXiv: 1410.8849 [hep-ph] (cit. on pp. 4, 39).

[13] ATLAS Collaboration, *ATLAS Pythia 8 tunes to 7 TeV data*, ATL-PHYS-PUB-2014-021, 2014, URL: https://cds.cern.ch/record/1966419 (cit. on pp. 4, 9, 44, 45).

[14] R. D. Ball et al., *Parton distributions with LHC data*, Nucl. Phys. B **867** (2013) 244, arXiv: 1207.1303 [hep-ph] (cit. on pp. 4, 5).

[15] M. Bahr et al., *Herwig++ physics and manual*, Eur. Phys. J. C **58** (2008) 639, arXiv: 0803.0883 [hep-ph] (cit. on p. 4).

[16] J. Bellm et al., *Herwig 7.0/Herwig++ 3.0 release note*, Eur. Phys. J. C **76** (2016) 196, arXiv: 1512.01178 [hep-ph] (cit. on p. 4).

[17] L. Harland-Lang, A. Martin, P. Motylinski and R. Thorne, *Parton distributions in the LHC era: MMHT 2014 PDFs*, Eur. Phys. J. C **75** (2015) 204, arXiv: 1412.3989 [hep-ph] (cit. on p. 4).

[18] J. Bellm et al., *Herwig 7.1 Release Note*, (2017), arXiv: 1705.06919 [hep-ph] (cit. on p. 4).

[19] J. Alwall et al., *The automated computation of tree-level and next-to-leading order differential cross sections, and their matching to parton shower simulations*, JHEP **07** (2014) 079, arXiv: 1405.0301 [hep-ph] (cit. on p. 4).

[20] S. Frixione, E. Laenen, P. Motylinski and B. R. Webber, *Angular correlations of lepton pairs from vector boson and top quark decays in Monte Carlo simulations*, JHEP **04** (2007) 081, arXiv: hep-ph/0702198 (cit. on p. 4).

[21] P. Artoisenet, R. Frederix, O. Mattelaer and R. Rietkerk, *Automatic spin-entangled decays of heavy resonances in Monte Carlo simulations*, JHEP **03** (2013) 015, arXiv: 1212.3460 [hep-ph] (cit. on p. 4).

[22] T. Gleisberg and S. Höche, *Comix, a new matrix element generator*, JHEP **12** (2008) 039, arXiv: 0808.3674 [hep-ph] (cit. on p. 4).

[23] S. Schumann and F. Krauss, *A Parton shower algorithm based on Catani-Seymour dipole factorisation*, JHEP **03** (2008) 038, arXiv: 0709.1027 [hep-ph] (cit. on pp. 4, 39).

[24] S. Höche, F. Krauss, M. Schönherr and F. Siegert, *A critical appraisal of NLO+PS matching methods*, JHEP **09** (2012) 049, arXiv: 1111.1220 [hep-ph] (cit. on p. 4).

[25] S. Höche, F. Krauss, M. Schönherr and F. Siegert, *QCD matrix elements + parton showers: The NLO case*, JHEP **04** (2013) 027, arXiv: 1207.5030 [hep-ph] (cit. on p. 4).

[26] S. Catani, F. Krauss, R. Kuhn and B. R. Webber, *QCD Matrix Elements + Parton Showers*, JHEP **11** (2001) 063, arXiv: hep-ph/0109231 (cit. on p. 4).

[27] S. Höche, F. Krauss, S. Schumann and F. Siegert, *QCD matrix elements and truncated showers*, JHEP **05** (2009) 053, arXiv: 0903.1219 [hep-ph] (cit. on p. 4).

[28] F. Buccioni et al., *OpenLoops 2*, Eur. Phys. J. C **79** (2019) 866, arXiv: 1907.13071 [hep-ph] (cit. on p. 4).

[29] F. Cascioli, P. Maierhofer and S. Pozzorini, *Scattering Amplitudes with Open Loops*, Phys. Rev. Lett. **108** (2012) 111601, arXiv: 1111.5206 [hep-ph] (cit. on p. 4).

[30] F. Buccioni, S. Pozzorini and M. Zoller, *On-the-fly reduction of open loops*, Eur. Phys. J. C **78** (2018) 70, arXiv: 1710.11452 [hep-ph] (cit. on p. 4).

[31] A. Denner, S. Dittmaier and L. Hofer, *Collier: A fortran-based complex one-loop library in extended regularizations*, Comput. Phys. Commun. **212** (2017) 220, arXiv: 1604.06792 [hep-ph] (cit. on p. 4).

[32] S. Kallweit, J. M. Lindert, P. Maierhöfer, S. Pozzorini and M. Schönherr, *NLO electroweak automation and precise predictions for W+multijet production at the LHC*, JHEP **04** (2015) 012, arXiv: 1412.5157 [hep-ph] (cit. on p. 4).

[33] S. Kallweit, J. M. Lindert, P. Maierhöfer, S. Pozzorini and M. Schönherr, *NLO QCD+EW predictions for V + jets including off-shell vector-boson decays and multijet merging*, JHEP **04** (2016) 021, arXiv: 1511.08692 [hep-ph] (cit. on p. 4).

[34] C. Gütschow, J. M. Lindert and M. Schönherr, *Multi-jet merged top-pair production including electroweak corrections*, Eur. Phys. J. C **78** (2018) 317, arXiv: 1803.00950 [hep-ph] (cit. on pp. 4, 39).

[35] D. J. Lange, *The EvtGen particle decay simulation package*, Nucl. Instrum. Meth. A **462** (2001) 152 (cit. on p. 5).

[36] M. Beneke, P. Falgari, S. Klein and C. Schwinn, *Hadronic top-quark pair production with NNLL threshold resummation*, Nucl. Phys. B **855** (2012) 695, arXiv: 1109.1536 [hep-ph] (cit. on p. 5).

[37] M. Cacciari, M. Czakon, M. Mangano, A. Mitov and P. Nason, *Top-pair production at hadron colliders with next-to-next-to-leading logarithmic soft-gluon resummation*, Phys. Lett. B **710** (2012) 612, arXiv: 1111.5869 [hep-ph] (cit. on p. 5).

[38] P. Bärnreuther, M. Czakon and A. Mitov, *Percent-Level-Precision Physics at the Tevatron: Next-to-Next-to-Leading Order QCD Corrections to $q\bar{q} \to t\bar{t} + X$*, Phys. Rev. Lett. **109** (2012) 132001, arXiv: 1204.5201 [hep-ph] (cit. on p. 5).

[39] M. Czakon and A. Mitov, *NNLO corrections to top-pair production at hadron colliders: the all-fermionic scattering channels*, JHEP **12** (2012) 054, arXiv: 1207.0236 [hep-ph] (cit. on p. 5).

[40] M. Czakon and A. Mitov, *NNLO corrections to top pair production at hadron colliders: the quark-gluon reaction*, JHEP **01** (2013) 080, arXiv: 1210.6832 [hep-ph] (cit. on p. 5).

[41] M. Czakon, P. Fiedler and A. Mitov, *Total Top-Quark Pair-Production Cross Section at Hadron Colliders Through $O(\alpha_S^4)$*, Phys. Rev. Lett. **110** (2013) 252004, arXiv: 1303.6254 [hep-ph] (cit. on p. 5).

[42] M. Czakon and A. Mitov, *Top++: A Program for the Calculation of the Top-Pair Cross-Section at Hadron Colliders*, Comput. Phys. Commun. **185** (2014) 2930, arXiv: 1112.5675 [hep-ph] (cit. on p. 5).

[43] J. Butterworth et al., *PDF4LHC recommendations for LHC Run II*, J. Phys. G **43** (2016) 023001, arXiv: 1510.03865 [hep-ph] (cit. on p. 5).

[44] A. D. Martin, W. J. Stirling, R. S. Thorne and G. Watt, *Parton distributions for the LHC*, Eur. Phys. J. C **63** (2009) 189, arXiv: 0901.0002 [hep-ph] (cit. on p. 5).

[45] A. D. Martin, W. Stirling, R. Thorne and G. Watt, *Uncertainties on α_S in global PDF analyses and implications for predicted hadronic cross sections*, Eur. Phys. J. C **64** (2009) 653, arXiv: 0905.3531 [hep-ph] (cit. on p. 5).

[46] H.-L. Lai et al., *New parton distributions for collider physics*, Phys. Rev. D **82** (2010) 074024, arXiv: 1007.2241 [hep-ph] (cit. on p. 5).

[47] J. Gao et al., *CT10 next-to-next-to-leading order global analysis of QCD*, Phys. Rev. D **89** (2014) 033009, arXiv: 1302.6246 [hep-ph] (cit. on p. 5).

[48] A. Buckley et al., *Rivet user manual*, Comput. Phys. Commun. **184** (2013) 2803, arXiv: 1003.0694 [hep-ph] (cit. on p. 6).

[49] ATLAS Collaboration, *Measurements of top-quark pair differential and double-differential cross-sections in the ℓ+jets channel with pp collisions at $\sqrt{s} = 13$ TeV using the ATLAS detector*, (2019), arXiv: 1908.07305 [hep-ex] (cit. on pp. 7, 9, 12, 14, 17, 18, 20, 24, 28, 35, 37, 38, 41–43, 46, 47).

[50] M. Cacciari, G. P. Salam and G. Soyez, *The Catchment Area of Jets*, JHEP **04** (2008) 005, arXiv: 0802.1188 [hep-ph] (cit. on p. 7).

[51] M. Cacciari, G. P. Salam and G. Soyez, *The anti-k_t jet clustering algorithm*, JHEP **04** (2008) 063, arXiv: 0802.1189 [hep-ph] (cit. on p. 7).

[52] ATLAS Collaboration, *Measurement of the $t\bar{t}$ production cross-section and lepton differential distributions in $e\mu$ dilepton events from pp collisions at $\sqrt{s}$ = 13 TeV with the ATLAS detector*, Eur. Phys. J. C **80** (2020) 528, arXiv: 1910.08819 [hep-ex] (cit. on pp. 7, 16, 20, 25, 29, 35, 36).

[53] ATLAS Collaboration, *Measurements of top-quark pair single- and double-differential cross-sections in the all-hadronic channel in pp collisions at $\sqrt{s}$ = 13 TeV using the ATLAS detector*, (2020), arXiv: 2006.09274 [hep-ex] (cit. on pp. 7, 12, 14, 15, 18, 20, 23, 27, 32–34).

[54] S. Frixione and B. R. Webber, *Matching NLO QCD computations and parton shower simulations*, JHEP **06** (2002) 029, arXiv: hep-ph/0204244 (cit. on p. 9).

[55] ATLAS Collaboration, *Measurements of top-quark pair spin correlations in the $e\mu$ channel at $\sqrt{s}$ = 13 TeV using pp collisions in the ATLAS detector*, Eur. Phys. J. C **80** (2020) 754, arXiv: 1903.07570 [hep-ex] (cit. on p. 9).

[56] ATLAS Collaboration, *Search for heavy particles decaying into a top-quark pair in the fully hadronic final state in pp collisions at $\sqrt{s}$ = 13 TeV with the ATLAS detector*, Phys. Rev. D **99** (2019) 092004, arXiv: 1902.10077 [hep-ex] (cit. on p. 9).

[57] *Les Houches 2017: Physics at TeV Colliders Standard Model Working Group Report*, 2018, arXiv: 1803.07977 [hep-ph] (cit. on p. 21).

[58] S. Hoeche, S. Schumann and F. Siegert, *Hard photon production and matrix-element parton-shower merging*, Phys. Rev. D **81** (2010) 034026, arXiv: 0912.3501 [hep-ph] (cit. on p. 39).

[59] E. Bothmann, M. Schönherr and S. Schumann, *Reweighting QCD matrix-element and parton-shower calculations*, Eur. Phys. J. C **76** (2016) 590, arXiv: 1606.08753 [hep-ph] (cit. on p. 39).